The quantification of down-hole fractionation for laser ablation mass spectrometry

Jarred C Lloyd[1, 2], Carl Spandler[1], Sarah E Gibert[3], and Derrick Hasterok[1]

[1]Department of Earth Science, The University of Adelaide, Australia
[2]Geological Survey of South Australia, Department for Energy and Mining, Government of South Australia, Australia
[3]Adelaide Microscopy, The University of Adelaide, Australia

Correspondence: Jarred C Lloyd (jarred.lloyd@adelaide.edu.au)

Abstract. Down-hole fractionation (DHF), a known phenomenon in static spot laser ablation, remains one of the most significant sources of uncertainty for laser-based geochronology. A given DHF pattern is unique to a set of conditions, including material, inter-element analyte pair, laser conditions, and spot geometry. Current modelling methods (simple or multiple linear regression, spline-based regression) for DHF do not readily lend themselves to uncertainty propagation, nor do they allow for

quantitative inter-session comparison, let alone inter-laboratory or inter-material comparison.

In this study, we investigate the application of orthogonal polynomial decomposition for quantitative modelling of LA-ICP-MS DHF patterns. We outline the algorithm used to compute the models, apply it to an exemplar U–Pb dataset across a range of materials and analytical sessions, and finally provide a brief interpretation of the resulting data.

In this contribution we demonstrate the feasibility of quantitative modelling and comparison of DHF patterns from multiple materials across multiple sessions. We utilise a relatively new data visualisation method, uniform manifold approximation and projection (UMAP), to help visualise the data relationships in this large dataset while comparing it to more traditional methods of data visualisation.

The algorithm presented in this research advances our capability to accurately model LA-ICP-MS DHF and may facilitate reliable decoupling of the DHF correction for non-matrix matched materials, lead to improved uncertainty propagation, and facilitate inter-laboratory comparison studies of DHF patterns.

The generalised nature of the algorithm means it is applicable not only to geochronology but also more broadly within the geosciences where predictable linear (x-to-y) relationships exist.

1 Introduction

LA-ICP-MS of geological materials has significantly advanced since its adoption at the end of the 20th century and is today the technique of choice for most applications for mineral geochronology. Initial geochronological studies on zircon were only able to produce tens of individual data per session due to technical, time, and computing limitations (e.g. Hirata and Nesbitt, 1995). Nowadays high-precision individual analyses on multiple minerals using a range of geochronologic systems (e.g. U–Pb, Rb–Sr, Lu–Hf, Re–Os) can be rapidly and accurately acquired (Chew et al., 2019; Gehrels et al., 2008; Glorie et al., 2023; Hogmalm et al., 2017; Kendall-Langley et al., 2020; Larson et al., 2024; McFarlane, 2016; Mohammadi et al., 2024; Roberts et al.,

25   2020; Simpson et al., 2021; Subarkah et al., 2021; Tamblyn et al., 2024; Zack et al., 2011). However, to achieve accurate, high-quality data, correction procedures need to be implemented, including calibration to reference material(s) (RM), corrections for matrix offsets, and inter-element down-hole fractionation (DHF) (Agatemor and Beauchemin, 2011; Allen and Campbell, 2012; Gilbert et al., 2017; Günther et al., 2001; McLean et al., 2016; Ver Hoeve et al., 2018). As DHF is a geometry-dependant spot-ablation phenomena unique to each material and (inter-element) analyte ratio pair (e.g. NIST SRM glasses, zircon, ^{206}Pb/^{238}U,

30   ^{207}Pb/^{235}U, ^{87}Rb/^{87}Sr) it cannot be corrected via ICP-MS tuning (Mank and Mason, 1999). However, DHF can be optimised to balance the overall count rate against the magnitude of DHF by adjusting the spot geometry and fluence parameters for analysis of a given material (Guillong and Günther, 2002; Košler et al., 2005). Researchers have proposed several methods for minimising DHF, typically by surface rastering or limiting acquisition times to short intervals; however, these compromise either the spatial or temporal resolution of analysis (Horstwood et al., 2003; Paton et al., 2010). Alternatively, regression

35   modelling can be used to correct DHF during the data reduction process either using a predetermined empirical model or fitting a model to the observed data (e.g. Horn et al., 2000; Paton et al., 2010). Currently, the latter method of fitting a regression model to the observed DHF pattern of a RM then applying that model to unknowns is used by commercial data reduction software (e.g. LADR: Norris and Danyushevsky, 2018; Iolite: Paton et al., 2011) for DHF correction in LA-ICP-MS methodology. In this process a matrix-matched RM is used (or a glass RM if no suitable matrix-matched material is available) and requires

40   the assumption that the unknowns (i.e. target samples) have the same DHF behaviour as the RM. If the modelled RM poorly matches the DHF of the unknown it will introduce some artefact (user induced error) that may either increase the uncertainty of the observed ratio of the unknowns if using a time matched signal, or result in over- or underestimation of the observed ratio if using a subset of the signal [Fig. 1].
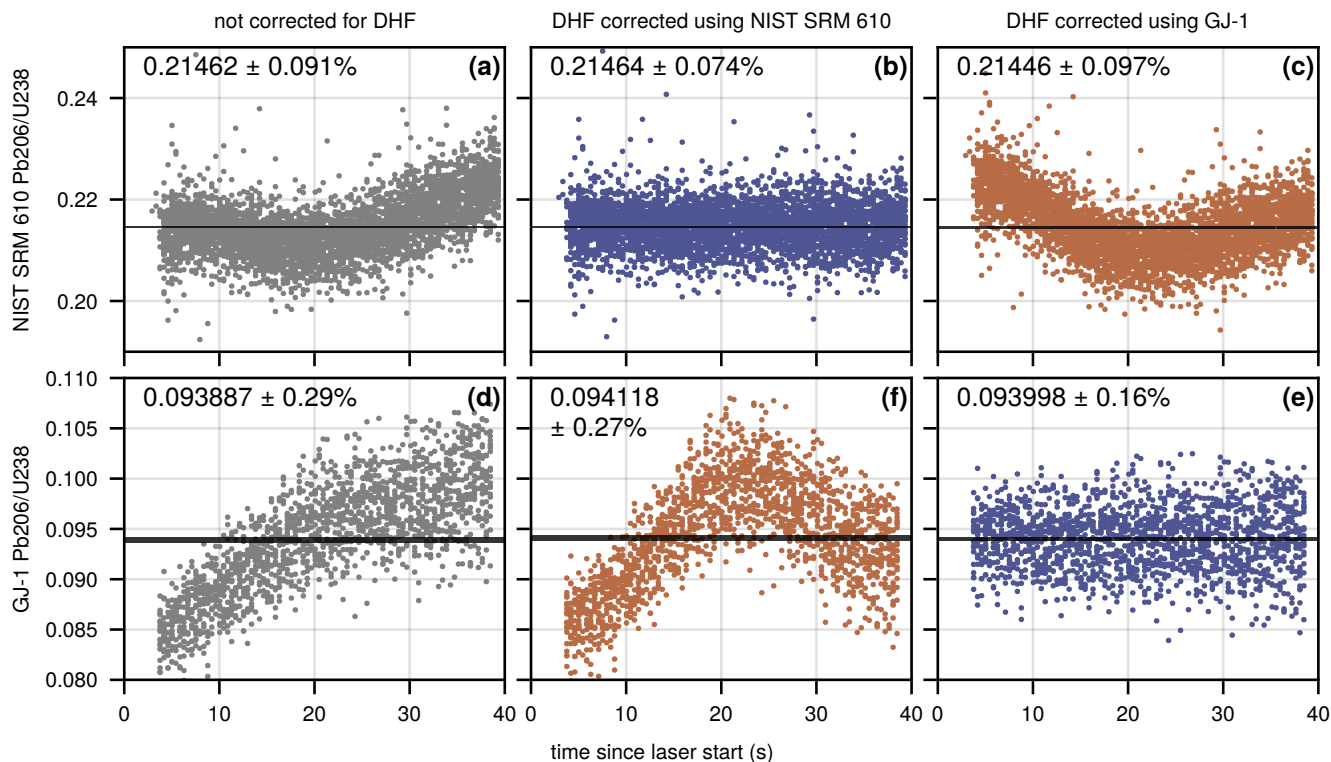
Figure 1. Demonstration of the impact of using an inappropriate material to correct down-hole fractionation (DHF). The two rows are [206]Pb/[238]U ratios for NIST SRM 610 glass (a–c) and GJ-1 zircon (d–f), respectively, collected in a single session. The columns from left to right are, not corrected for DHF (grey points, raw ratios), DHF corrected using NIST SRM 610 as the model, and DHF corrected using GJ-1 as the model. Blue points indicate an appropriate DHF correction (e.g. GJ-1 by GJ-1) while orange points indicate an inappropriate DHF correction (e.g. GJ-1 by NIST SRM 610). Black horizontal spans indicate the geometric mean and its asymmetric lower and upper 2-standard error for each data set. The percent error shown is 2-standard error level of the larger geometric standard error (usually upper uncertainty). Note the significantly larger error for the inappropriate corrections (orange points) compared to the appropriate (blue) corrections. These uncertainties would then propagate into further processing steps to obtain accurate LA-ICP-MS ratios (e.g. calibration to a known value).

Additionally, these modelling methods (i) do not readily lend themselves to arithmetic propagation of their uncertainties (Paton et al., 2010), (ii) require an arbitrary user choice for the fitting method (simple or multiple linear regression polynomial order, or non-linear regression), and (iii) cannot be quantitatively compared between laboratories or even intra-laboratory analytical sessions. Thus, inter-element DHF remains one of the largest sources of uncertainty for LA-ICP-MS analyses and is difficult to either qualitatively or quantitatively compare (Horstwood et al., 2016).

Here we present a technique to numerically quantify processes in the geosciences which can be modelled by a linear combination of basis functions (e.g. DHF) using the coefficients of orthogonal polynomials fit to the signals. We develop upon the algorithms for quantitative modelling of rare earth element patterns by O'Neill (2016) and Anenburg and Williams (2022). Our modified implementation of these algorithms uses input uncertainties as weights and can be more generally applied to data where there is a predictable x-to-y relationship. Here we demonstrate the technique's application for modelling DHF in a quantitative manner.

Using a LA-ICP-MS dataset (time, ratio of analytes), an orthogonal decomposition is used to fit a polynomial to the signal data by generalised least-squares [Fig. 2]. This method of using orthogonal polynomial decomposition during model fitting enables the quantitative comparison of DHF patterns via their coefficients for data from different analyte ratio pairs, for varied materials, and for inter-session [Fig. 2] and inter-laboratory datasets. Furthermore, this fitting method allows for improved computation of the uncertainty for each coefficient (and thus overall fit) and their covariances which can then be propagated into the final result.

In this research we highlight the utility of the algorithm for numeric comparison of the U–Pb DHF patterns from a range of natural and synthetic RMs used for U–Pb age date calibration. We envisage that this algorithm could be used to self-correct individual analyses for DHF (or as spline bases for signals that display zonation, e.g. different age domains), with a fall back to a known RM in the case of particularly noisy (analytical noise) data. This would allow reliable decoupling of the DHF correction for non-matrix matched materials, and propagation of the uncertainty in the down-hole model into the result, thereby improving the accuracy and precision of LA-ICP-MS analyses.
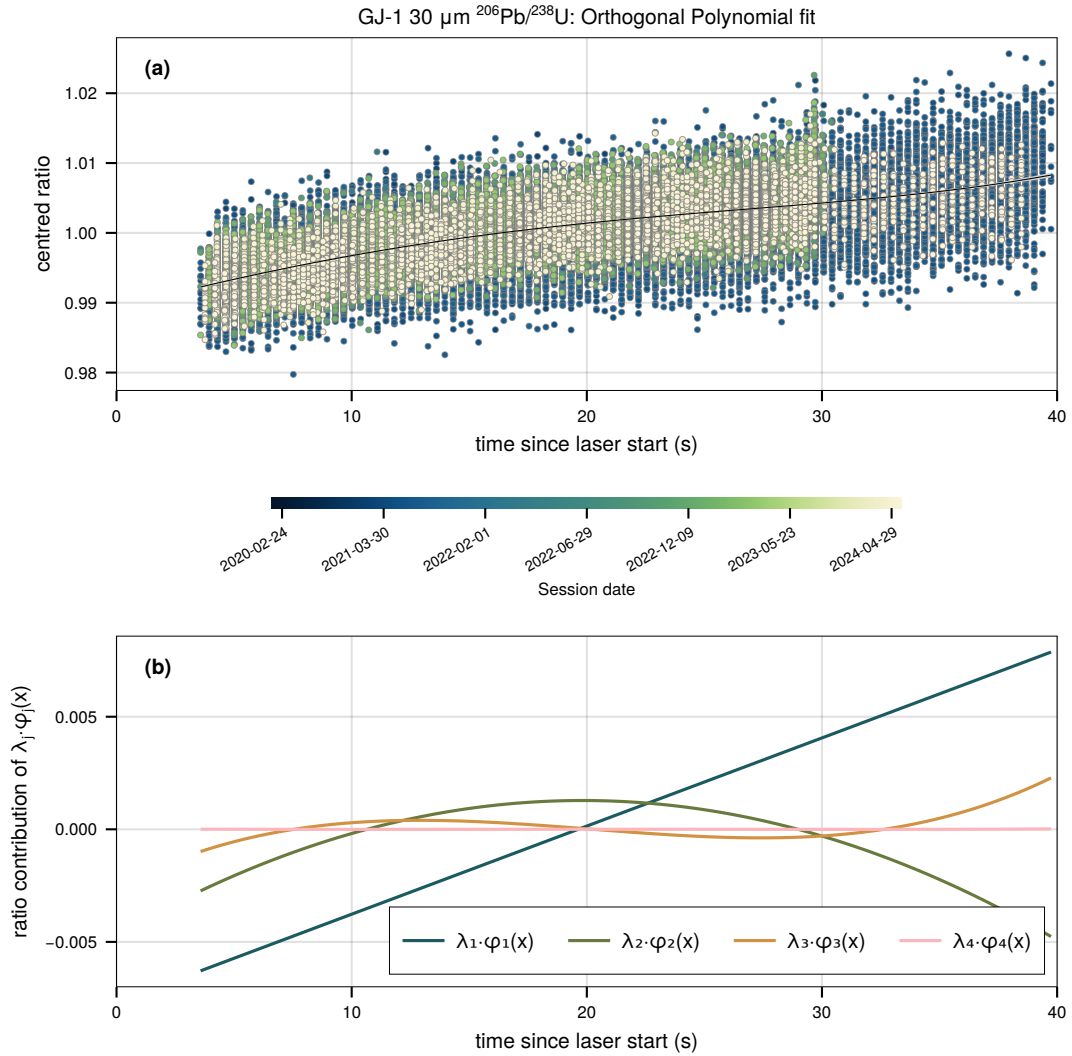
Figure 2. (a) Centred, point-wise $^{206}Pb/^{238}U$ ratios for all zircon GJ-1 analyses measured in multiple analytical sessions from 2020 to 2024 that used the same laser parameters. All analyses in this subset of data were collected using a 30 µm spot diameter, 5 Hz repetition rate, and nominal fluence of 2.0 Jcm^{-2}. The black line is the fitted orthogonal polynomial, with grey shading indicating the 95% confidence interval of the fit. The shaded confidence interval is barely visible due to its small absolute range. (b) Individual orthogonal components (i.e. the result of $\lambda_j \cdot \varphi_j(x)$) of the fit in the upper panel excluding λ_0 (mean ratio, i.e. vertical central tendency) as this is a function of mass-spectrometer tuning and not a result of down-hole fractionation (DHF). φ_j is the orthogonal function evaluated at x^j (i.e. $x^0, x^1, x^2, \ldots$) for $j = 1$ to order k. For this aggregated GJ-1 data, different mass-spectrometer tuning parameters and drift are accounted for by centring the data (subtraction of geometric mean and adding a constant of 1) resulting in $\lambda_0 \approx 1$. Components λ_1 and higher represent the increasing shape component (linear slope, quadratic curvature, etc.) of the observed DHF pattern. Note, in this case the magnitude of λ_4 is approximately zero, as such, the result of λ_4 is approximately a horizontal line at zero. The sum of all components forms the polynomial in the upper panel.

2 Experimental

To improve our ability to assess, quantify, and compare DHF we implement a method of orthogonal polynomial decomposition to perform multiple linear regression (polynomial) model fitting to time-resolved analytical data from ICP-MS instruments. In keeping with the terminology of O'Neill (2016) and Anenburg and Williams (2022) we use the term lambda (λ) coefficients to denote the polynomial coefficients derived from models using orthogonal decomposition.

Unlike regular linear regression fitting, the implementation of orthogonal polynomial decomposition for regression modelling imparts the property of independence on lower order polynomial coefficients from their higher order counterparts (Bevington and Robinson, 2003). That is, the first coefficient is independent of the second and higher order coefficients, while the second coefficient is independent of the third and higher order coefficients and so forth. In practice, this means that the values of the polynomial coefficients are stable (you can fit a first or second order polynomial to some data and the value of first coefficient will not change) and they have some physical meaning in relation to the data. In the case of DHF data, λ_0 (the first coefficient) represents the (arithmetic) mean ratio, while λ_1 and higher are the shape parameters that represent the DHF pattern [Fig. 2]. For example, λ_1 represents the linear slope (mean rate of change in ratio) while λ_2 represents the quadratic curve of the DHF pattern [Fig. 2]. The independence and physical meaning of the lambda coefficients allows them to be used to quantitatively compare independent fits (e.g. single analyses, materials, analytical sessions, differing laboratories) so long as other parameters (e.g. fluence, spot diameter/volume, laser wavelength) are considered. Further details on the fitting algorithm and mathematics behind this process are outlined below in Sect. 2.2, detailed in Appendix A, and described in Bevington and Robinson (2003), O'Neill (2016), and Anenburg and Williams (2022). The raw data ingestion and required preprocessing steps are outlined below in section Sect. 2.1.

Code written to perform the data ingestion, preprocessing, and fitting were written in the Julia (version 1.10, LTS) programming language (Bezanson et al., 2017). The code forms part of an in-development Julia package, GeochemistryTools.jl that will be formally released in the future. Should users want early access to the package or source code for the algorithms outlined in this manuscript they are available via GitHub (see code and availability). Figures were generated using the Makie.jl plotting library (Danisch and Krumbiegel, 2021) using "Scientific colour maps" (Crameri et al., 2020) implemented in ColorSchemes.jl.

2.1 Data ingestion and preprocessing

Data were imported from the raw ICP-MS CSV files; in this case from Agilent ICP-MS instruments. The algorithm written for this task processes the individual files (which can be a single analysis, a specified sample, or entire session) and performs several operations, outlined in Fig. 3, on user-specified mass counts-per-second (CPS) columns (i.e. channels, analyte signals).
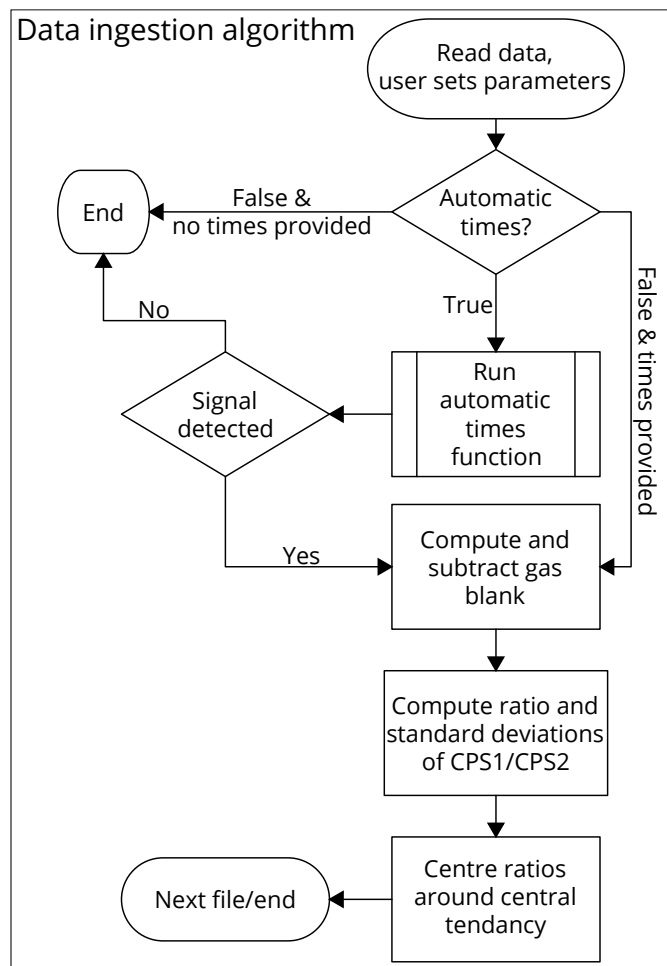
Figure 3. Outline of data ingestion algorithm. CPS = counts-per-second of analyte (e.g. ^{238}U).

95   An automated procedure for determining gas blank and signal windows, as well as laser fire time, and aerosol arrival was developed to aid in rapid data processing and quality control. This algorithm is outlined in Fig. S1 with examples of the automatically determined time points and signal windows shown in Fig. S2.

Gas blank determination uses a geometric mean adapted for zeros [Eq. 1] as per Habib (2012),

$$\text{for } G \geq 0, \; G = \frac{n_+ G_+ + n_0 G}{N} = \frac{n_+}{N} G_+ \tag{1}$$

100   where G is the geometric mean, N is the total count of data, x_i is the i-th input value from $i = 1$ to $i = N$, G_+ is the geometric mean of all $x_i > 0$, n_+ is the count of $x_i > 0$, G_0 is the geometric mean of all $x_i = 0$ (i.e. 0), and n_0 is the count of all $x_i = 0$.

As previously outlined (Sect. 2) the nature of orthogonal polynomial decomposition means that lambda coefficients (and their uncertainties) one and higher should not change with respect to a centred or non-centred dataset for a single analysis. For aggregated data (session and/or sample aggregation), higher order lambda coefficients of centred and non-centred may not

105   be equal unless all external factors (fluence, spot-diameter, machine drift) have been controlled for. We strongly recommend that centred datasets are used for fitting intra- and intersession sample aggregated datasets as the centring process will remove the influences of machine drift and tuning that λ_0 is sensitive to. Aggregation of data requires grouping by factors known to influence DHF (see Sect. 3.1) to ensure like-for-like data is being modelled.

Centring of the data aligns the central tendencies of each individual analysis to ≈ 1 while retaining the scale and shape [Fig.

110   4] of the change in raw ratios over the time-resolved signal, i.e. the DHF. Centring is performed by subtracting the central tendency (i.e. geometric mean, or a user could alternatively use the arithmetic mean, or median) from the time-resolved ratios for each individual file (i.e. analysis) and adding a constant value of 1.0 to the result. The addition of the constant to centre the values around one is to prevent numeric errors during weighted fits when the weights (input errors) are very small (i.e. close to 0). This centring enables visual comparison [Fig. 4] and accurate numeric assessment of DHF behaviours across samples,

115   sessions, spot geometries, and fluences without the need to calibrate data to a known RM ratio for each session or accounting for machine drift during a session.
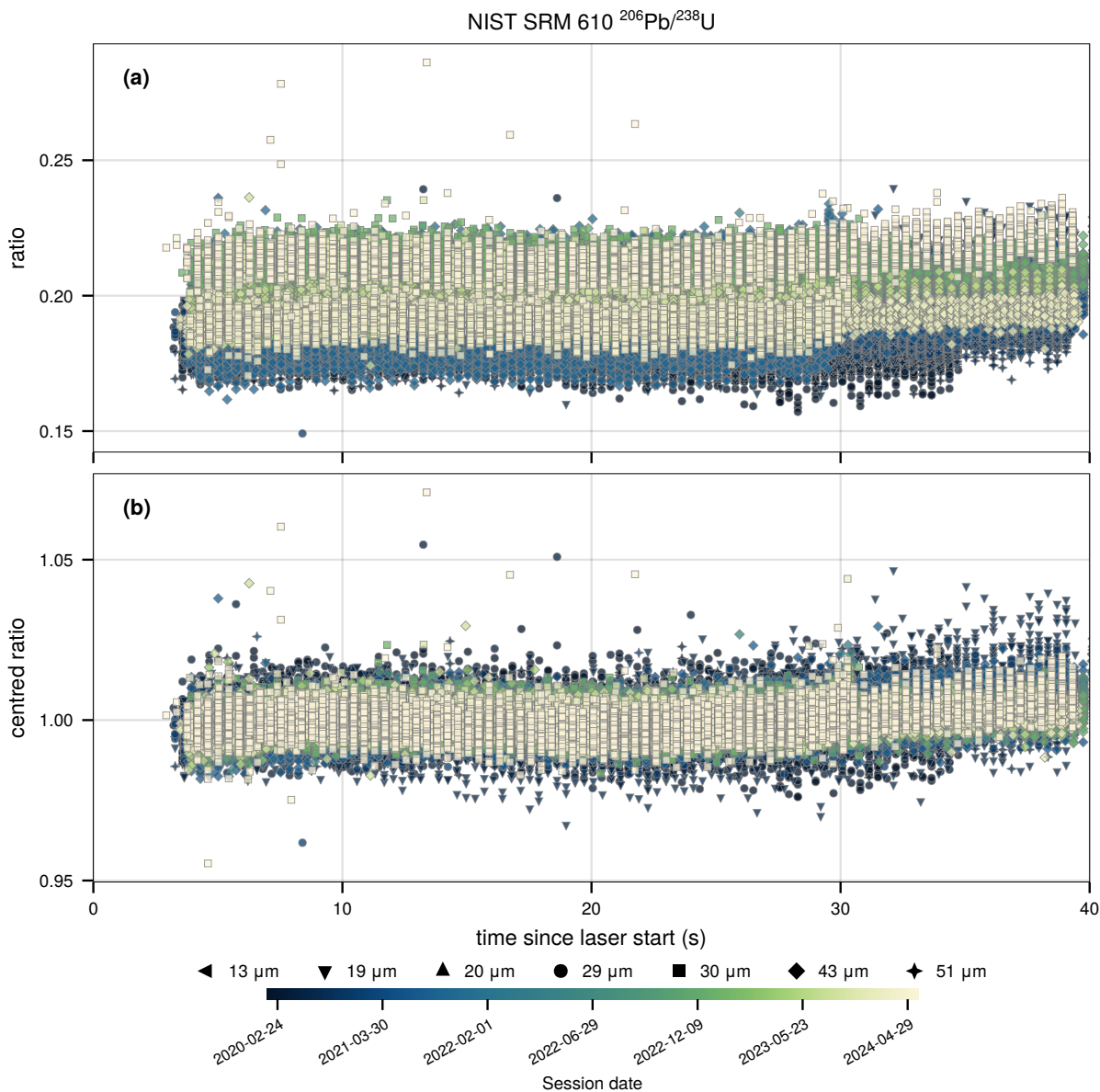
Figure 4. (a) Point-wise computed $^{206}Pb/^{238}U$ ratios for each measurement of NIST SRM 610 glass in the dataset. Symbol shapes represent spot-diameter and colour represents date of analytical session. (b) Centred point-wise $^{206}Pb/^{238}U$ ratios for each measurement of NIST SRM 610 glass in the dataset (same data as in (a)). Centring (by subtraction of geometric mean and adding a constant of 1) preserves the relative positions of each data point but aligns them to a common central tendency. This preserves the shape and scale of the DHF pattern while removing ICP-MS tuning and drift effects, thus allowing accurate comparison between measurements using differing laser parameters, measurements on different materials, and across ICP-MS sessions or laboratories.

2.2 Outline of fitting algorithm

In the following equations x denotes the independent variable (e.g. time in seconds) and the dependant variable (e.g. analyte ratio) is represented by y for observed values or $\hat{y}$ for predicted values of some function of x, i.e. $f(x)$. For clarity, we use φ to differentiate the orthogonal function terms and λ to differentiate the coefficients of the orthogonal polynomial from their regular counterparts (f and β respectively). Function terms and coefficients use j and l as indices with k denoting the polynomial order. The indicator i is used for the i-th value of x_i, y_i, and $\hat{y}_i$ for $i = 1$ to $i = N$ (total count of data).

Polynomials of order k [Eq. (2)] can be orthogonal to each other under some inner product [Eq. (3)]. The property of independence of each coefficient also enables efficient computation of the polynomial statistics (errors, variances and covariances, residual sum of squares etc.) at each order. The efficient computation is enabled because only the coefficient matrix of the highest order (five in our case) needs to be calculated, rather than the entire solution for each polynomial order. Once computed, subsequent calculations can use specific subsets of the operator and coefficient matrices to determine predictions and statistics for each polynomial order.

$$F(x) = \beta_0 + \sum_{j=1}^{k} [\beta_j f_j(x)] \tag{2}$$

$$\langle f_j(x), f_l(x) \rangle = 0 \text{ for } j \neq l \tag{3}$$

$$\Phi(x) = \lambda_0 + \sum_{j=1}^{k} [\lambda_j \varphi_j(x)] \tag{4}$$

In this contribution, we apply this to the DHF observed during LA-ICP-MS using the orthogonal property in Eq. 5.

$$\sum [\varphi_j(x_i) \varphi_l(x_i)] = 0 \text{ for } j \neq l \tag{5}$$

We construct a fourth-order polynomial function [Eq. (6)] using the sum of a set of orthogonal polynomials (Anenburg and Williams, 2022; Bevington and Robinson, 2003; O'Neill, 2016).

$$\hat{y}(x_i) = \lambda_0 + \lambda_1 \varphi_1(x_i) + \lambda_2 \varphi_2(x_i) + \lambda_3 \varphi_3(x_i) + \lambda_4 \varphi_4(x_i) \tag{6}$$

The orthogonal functions are solved for by using the methods outlined in Anenburg and Williams (2022) which make use of Vieta's formula and polynomial root finding. See Anenburg and Williams (2022), Appendix A, or the source code for further detail. Once the orthogonal polynomial forms are computed, the algorithm generates the operator matrix $\mathbf{X}$ and uses generalised least-squares regression [Eqs (7) to (9)] to solve the vector $\boldsymbol{\lambda}$, and matrix $\mathbf{U}$, while utilising analytical uncertainties ($\boldsymbol{\epsilon}$) for weights. The vector $\boldsymbol{\lambda}$ contains the polynomial coefficients $\lambda_0 \ldots \lambda_4$, while the matrix $\mathbf{U}$ contains the variances and

covariances. Scaled values of ϵ are used to construct the diagonal values of the weight matrix $\mathbf{\Omega}$.

$$y = \mathbf{X}\boldsymbol{\lambda} + \boldsymbol{\epsilon}, \ E\left[\boldsymbol{\epsilon}|\mathbf{X}\right] = 0, \text{ and } Cov\left[\boldsymbol{\epsilon}|\mathbf{X}\right] = \sigma^2\mathbf{\Omega}^{-1} = \mathbf{U} \tag{7}$$

$$\boldsymbol{\lambda} = \left(\mathbf{X}^\mathsf{T}\mathbf{\Omega}^{-1}\mathbf{X}\right)^{-1}\mathbf{X}^\mathsf{T}\mathbf{\Omega}^{-1}y \tag{8}$$

$$\mathbf{U} = \left(\mathbf{X}^\mathsf{T}\mathbf{\Omega}^{-1}\mathbf{X}\right)^{-1} \tag{9}$$

$$\tag{10}$$

A graphical representation of the individual orthogonal polynomial components and an example of the resulting fit is shown in Fig. 2. Our algorithm allows the user to employ automated outlier removal with an outlier considered to have a studentised residual ≥ 3. The residuals used in outlier identification are computed from the orthogonal polynomial order with the minimum Akaike Information Criteria corrected (AICc) value [Eq. (11)] (Akaike, 1974; Burnham and Anderson, 2002). If outlier removal is enabled, the algorithm will iterate over the input data until no studentised residuals ≥ 3 remain in the fit, or it has gone through ten iterations. The minimum AICc is used to determine the 'best fit' (i.e. minimum information loss) polynomial order for each dataset.

$$\text{AICc} = n\log\left(\frac{\text{rss}}{n}\right) + 2k + \frac{2k\left(k+1\right)}{n-k-1} \tag{11}$$

where k is the order plus two, n is the count of data, and rss is the residual sum of squares for the model. Several measures of fit are computed and accessible to the user via the object created during the fitting algorithm. These measures include the Bayesian Information Criteria corrected (BICc), the AICc and BICc weights, the normalised root-mean-square error, the reduced chi-squared statistic χ_r^2, the multiple correlation coefficient ρ^2 or R^2 value, and an unbiased Olkin-Pratt adjusted estimator ρ_{OP}^2 of ρ^2 (Karch, 2020; Olkin and Pratt, 1958). Further detail can on these measures of fit be found in Appendix A.

An additional consideration in this algorithm is that floating point computation is inherently inexact, has finite precision and can incur round-off errors (Fernández et al., 2003). While round-off errors are not an issue with most geochemical computations generally, due to the often-small absolute values and numerous sequential computations being performed in this algorithm, these errors can lead to inaccuracy in the result. To overcome these potential accuracy issues we utilise the extended precision library MultiFloats.jl (Zhang, 2024) alongside Julia's native extended precision operations. We also use QR Factorisation or singular-value-decomposition (SVD) depending on the condition number of the operator matrix to solve for the $\boldsymbol{\lambda}$ vector and the variance-covariance $\mathbf{U}$ matrix to ensure numeric stability. If, after the final calculation, the absolute value of a coefficient is less than the default machine rounding tolerance for the extended precision type (Float64x4) it is rounded to zero as it is considered to be unresolvable from a value of zero.

2.3 Analysis of reference materials by LA-ICP-MS

Reference materials for apatite (401, KO, MAD, Durango, Wilberforce), baddeleyite (BADPHE, G15874, G18650), monazite (TS1MNZ, 222, RW1, MAdel, MtGar, Ambat), rutile (R10, R19), titanite (Mt Painter, MKED), xenotime (MG1, BS1), and zircon (Mud Tank, Plešovice, GJ-1, 91500, Temora, Rak17) were analysed for U–Pb isotope ratios and trace element concentrations using optimal methods for the specific mineral (Bockmann et al., 2022; Fletcher et al., 2004; Gain et al., 2019; Glorie

et al., 2020; Hall et al., 2018; Horstwood et al., 2016; Liu et al., 2011; Lloyd et al., 2022; Payne et al., 2008; Sláma et al., 2008;

175 Spandler et al., 2016; Thompson et al., 2016; Wiedenbeck et al., 2004; Yang et al., 2024). An additional monazite (Pilbara) and several potential cassiterite (in-house) RMs were also measured. Samples were analysed using a RESOlution-LR 193 nm ArF excimer laser ablation system coupled to an Agilent 8900 ICP-MS/MS. Both instruments are housed at The University of Adelaide within the analytical facilities at Adelaide Microscopy. Full metadata for LA-ICP-MS analysis can be found in Appendix B.

180 Additional zircon, rutile, and baddeleyite RM data from prior studies were added to supplement the dataset and allow the assessment of the viability of inter-session comparison (Lloyd et al., 2020, 2022, 2023, 2024; van der Wolff, 2020; Yang et al., 2024). These supplemental data were collected using the same LA system, coupled to either an Agilent 7900 ICP-MS (prior to November 2021) or the Agilent 8900 ICP-MS/MS in single quadrupole mode (from November 2021). Analytical conditions for these additional data can be found in the relevant references.

3   Results and discussion

In total, 5478 analyses (CSV files) were processed and their DHF patterns were modelled with the orthogonal polynomial decomposition outlined above (Sec. 2.2). This results in 5478 analysis fits, 188 session fits (sample aggregated per session), and 58 sample fits (sample aggregated across all sessions) accounting for differences in spot geometry across 29 unique materials [Fig. 5 & Fig. 6].

190 Linear slopes for the sample fits (λ_1) range from -5.88×10^{-5} to $0.0217 \, \text{s}^{-1}$, quadratic curvatures (λ_2) range from -3.06×10^{-5} to $3.27 \times 10^{-5} \, \text{s}^{-2}$, cubic curvatures ($\lambda_3$) range from -9.76×10^{-6} to $1.91 \times 10^{-5} \, \text{s}^{-3}$, and quartic curvatures (λ_4) range from -4.23×10^{-6} to $3.82 \times 10^{-7} \, \text{s}^{-4}$. Given the small numbers and large quantity of fits, it is not feasible to display a table with all parameters nor is it intuitive for the reader. Instead, we provide the visual representation of λ_1 plotted against λ_2 and their best fit uncertainties (2-standard error) in Fig. 5, as well as the visual polynomial fit and its uncertainty for the sample fits

195 in Fig. 6.
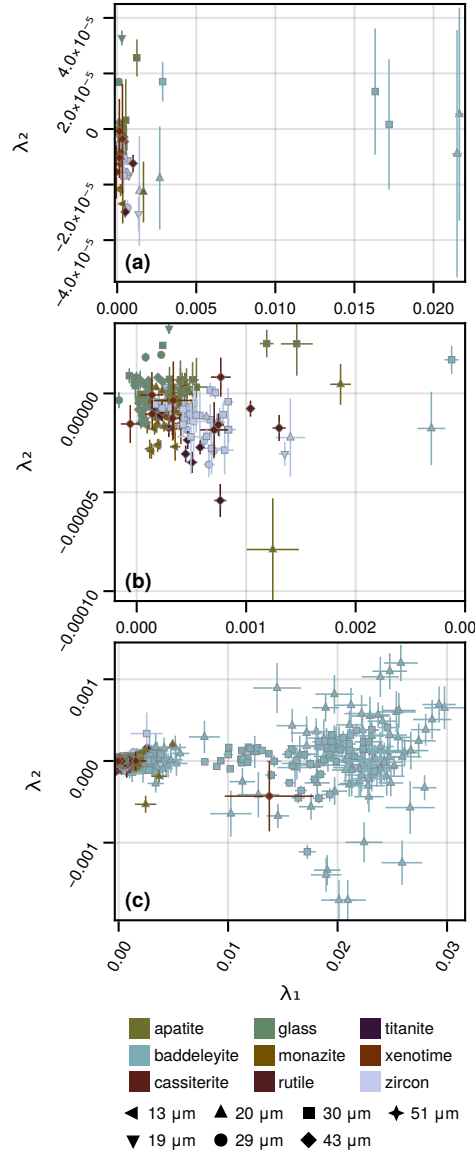
Figure 5. Scatter plot of λ_1 (x-axis) and λ_2 (y-axis) for sample-aggregated (a), session-sample-aggregated (b), and individual analysis (c) orthogonal polynomial fits. Symbol shapes represent spot-diameter and symbol colour represents material type. Uncertainty bars are 2-standard error. Fits with a greater positive linear slope will plot further to the right, and fits with a greater quadratic curvature will plot to higher (positive) or lower (negative) positions on the y-axis. In these simple bi-plots it can be readily observed that distinguishing between points becomes difficult or near impossible when many data are plotted, or there is large variation in some data.
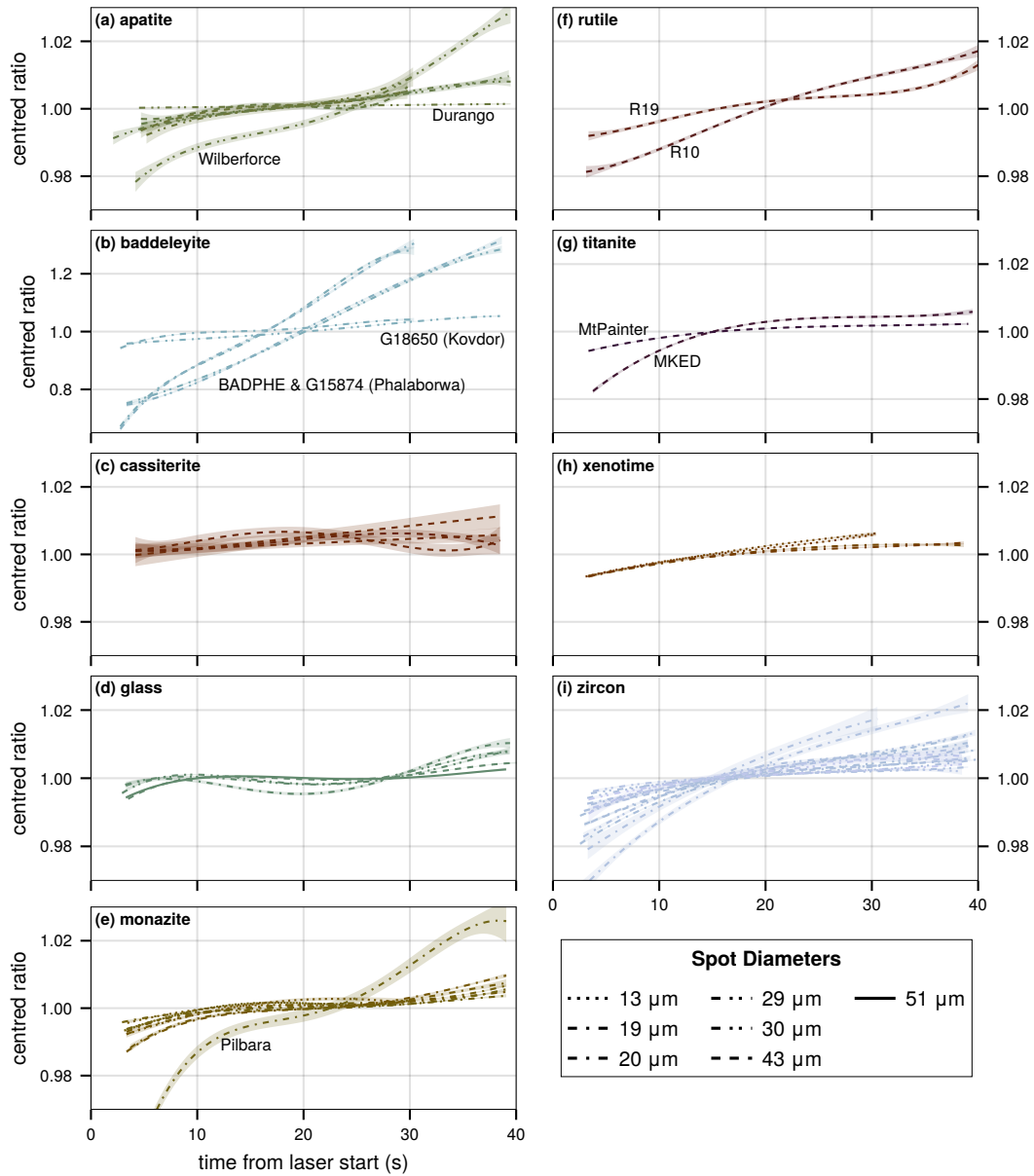
Figure 6. Orthogonal polynomial fits of down-hole fractionation (^{206}Pb/^{238}U) grouped by sample material. Note that the baddeleyite has a significantly larger y-axis scale due to the steeper linear fractionation component. Shaded areas show the 95% confidence interval of the individual fit. Increasing line solidity corresponds to increasing spot diameters.

3.1 Factors affecting down-hole fractionation

The scope of this contribution is to provide a tool that can be used for quantitative modelling of DHF and not an assessment of factors that influence DHF. Nonetheless, it is worth highlighting what the influencing factors are, and what considerations are needed for accurately using the proposed method to model these patterns. As stated earlier, DHF is a phenomenon observed in LA-ICP-MS (and other mass spectrometry methods) where the observed inter-element isotopic ratios change as a function of ablation depth/time independent of geological heterogeneity. This phenomenon is known to have several contributing factors and their interactions are complex (Guillong and Günther, 2002; Günther et al., 1997; Hergenröder, 2006a, b; Horn et al., 2000; Košler et al., 2005; Kroslakova and Günther, 2006; Mank and Mason, 1999; McLean et al., 2016; Paton et al., 2010; Sylvester and Ghaderi, 1997; Ver Hoeve et al., 2018). It is known that sample material, spot diameter–depth ratio/geometry, laser wavelength, fluence, laser repetition rate, and analyte volatilities all noticeably influence the observed down-hole inter-element isotopic ratio. Thus, careful consideration of these parameters is needed when performing any modelling of the observed patterns. For example, it would not be sensible to combine data from two analyses of the same material that have different laser repetition rates and model that combined data, as a priori knowledge dictates that we would observe different DHF patterns over the same time interval from the two separate analyses. As such, when aggregating data in this current study, we ensure that only like-for-like data are combined, e.g. same material using the same laser wavelength with the same laser parameters (spot geometry, repetition rate, fluence) within a small tolerance (e.g. nominally 2.0 Jcm^{-2} ± 0.1 Jcm^{-2}). Future studies could assess what a suitable tolerance is for each parameter; however, tolerances used in the current study (e.g. ± 0.1 Jcm^{-2}) do not appear to cause spurious results.

3.2 Physical interpretation of λ coefficients

Without needing RM calibration, the derived coefficients (λ_1 and higher) represent numerical parameters of DHF patterns for any given analysis Fig. 2.

The first coefficient, λ_0 will inherit the units of the y-variable. For this study, the value is unitless due to the y-variable being $\frac{\mathrm{CPS}}{\mathrm{CPS}}$ but can be interpreted as the mean of y, i.e. the mean ratio. As we are centring all data around a value of one to remove the influence of machine calibration and drift λ_0 has limited use in this research contribution; however, it could be used to calculate machine drift, and the nominal correction value for known-ratio materials (ICP-MS mass-bias correction) during data reduction. The second coefficient, λ_1, has units of s^{-1} and can be interpreted as the average rate of change/overall magnitude of change of the ratio between two analyte intensities over time. We suggest that this component largely reflects the fractionation occurring as a result of the change in depth-to-radius ratio during ablation. The third coefficient, λ_2, has units of s^{-2} and can be interpreted as the acceleration (or deceleration) in the rate of change of the ratio over time. We propose that fractionation due to differences in the relative volatilities of the analytes is the major control on this component, i.e. the analyte signal intensities decaying at different rates as the depth-to-radius ratio increases.

Higher order terms have more complex meanings, they are subsequent derivatives of the prior term. The fourth coefficient, λ_3, has units of s^{-3} and can be interpreted as the rate of change in the acceleration (λ_2) of the ratio rate of change through

time. This is likely reflecting the focussing of the laser induced plasma as the hole geometry changes and causes subsequent change in shape of the ablation plume from the ablation site. It will be represented by an inflection point in the signal (i.e. free surface expansion to increased crater wall interaction). The fifth coefficient, λ_4, has units of s^{-4} and can be interpreted as the rate of change of λ_3 over time. We believe this term could be incorporating detector effects such as electrical noise, low signal-to-background ratios, and Poisson noise at low signal intensity.

From the above reasoning, we expect that a third order polynomial ($\Phi_3(x)$, $\lambda_{1...3}$) should account for most of the variation seen in ratios over time during static spot ablation as a function of the ablated material and measured analytes. The fifth term (fourth order polynomial) should incorporate the remaining contributions to the fit but are likely to be a result of instrument induced artefacts.

3.3   Data analysis and visualisation

The proposed algorithm can efficiently handle large datasets, generating substantial numeric data. This presents two challenges; 1) analysing the data as it becomes a "big data" problem, and 2) visualising the data in a meaningful and interpretable way.

There exists well established literature for the analysis of large and/or multidimensional datasets. For multivariate data there is often a transformation from a higher-dimensional space to a lower-dimensional space to enable univariate and bivariate statistics. For example, methods such as principal-component-analysis (PCA) may be used to numerically evaluate the multivariate datasets.

Visualisation of multidimensional and/or large datasets is challenging. For simple two-dimensional data, an analyst can produce biplots (x–y scatter plots) to visualise any relationships in data. For three- and four-dimensional data, analysts can plot either ternary or quaternary diagrams which require mathematical transformations of the data into a lower dimension (e.g. 3-d to 2-d) that emulate the higher order space; hence, are increasingly complex to visualise and interpret. In all cases large datasets can lead to visual clutter (over-plotting) where the viewer will not be able to readily distinguish between similarly positioned data points.

In Fig. 5 we have plotted λ_1 on the x-axis and λ_2 on the y-axis, with corresponding uncertainty bars (2SE). These plots are limited to displaying only two of the five coefficients, and suffer from visual clutter where it is difficult to distinguish some point from another and from scaling issues where the variation in some data is responsible for obscuring the view of other data.

Alternatively an analyst can employ dimensional reduction visualisation methods such as PCA, multidimensional scaling (MDS), or uniform manifold approximation and projection (UMAP) to visualise the higher-dimensional data in a lower dimensional space. PCA can still incur visual clutter as multiple reduced components may still share the same coordinates, and PCA may not always be able to reduce the data to only two or three principal components that explain the majority of variance in a dataset. Conversely, UMAP will always be able to reduce a dataset to a specified number of dimensions and has hyperparameters that enhance visualisation to eliminate visual clutter.

We utilise UMAP [Fig. 7] to visualise the relative relationships of the higher dimensional data in a lower dimensional space (McInnes et al., 2020). UMAP takes the input multidimensional data (5478×4 λ coefficients in this study) and tries to find a common embedding space (using the manifold assumption) to represent the local and global data topology in a

lower dimension. UMAP has several variables called hyperparameters which control the output of the algorithm. The n-nearest neighbours hyperparameter is the most important for finding the balance between the global (low n-n) and local (high n-n) data

265 structure. We use a value of 19 for the n-nearest neighbours hyperparameter as the minimum number of analyses for a single material in a session is 20, so we expect there to be 19 related points. We set the minimum distance hyperparameter to 1.0 to push the points apart to help visualisation.

In simpler terms, UMAP works by constructing a graph in high-dimensional space (e.g. 4-dimensional) that is projected onto a lower-dimensional space (e.g. 2-dimensional) where points are connected based on their closeness in higher-dimensional

270 space. The shape of the data clusters in UMAP is a manifestation of the spatial relationships between higher-dimensional data with similar attributes and is not directly interpretable in a physical manner like traditional bi-plots or PCA (McInnes et al., 2020).
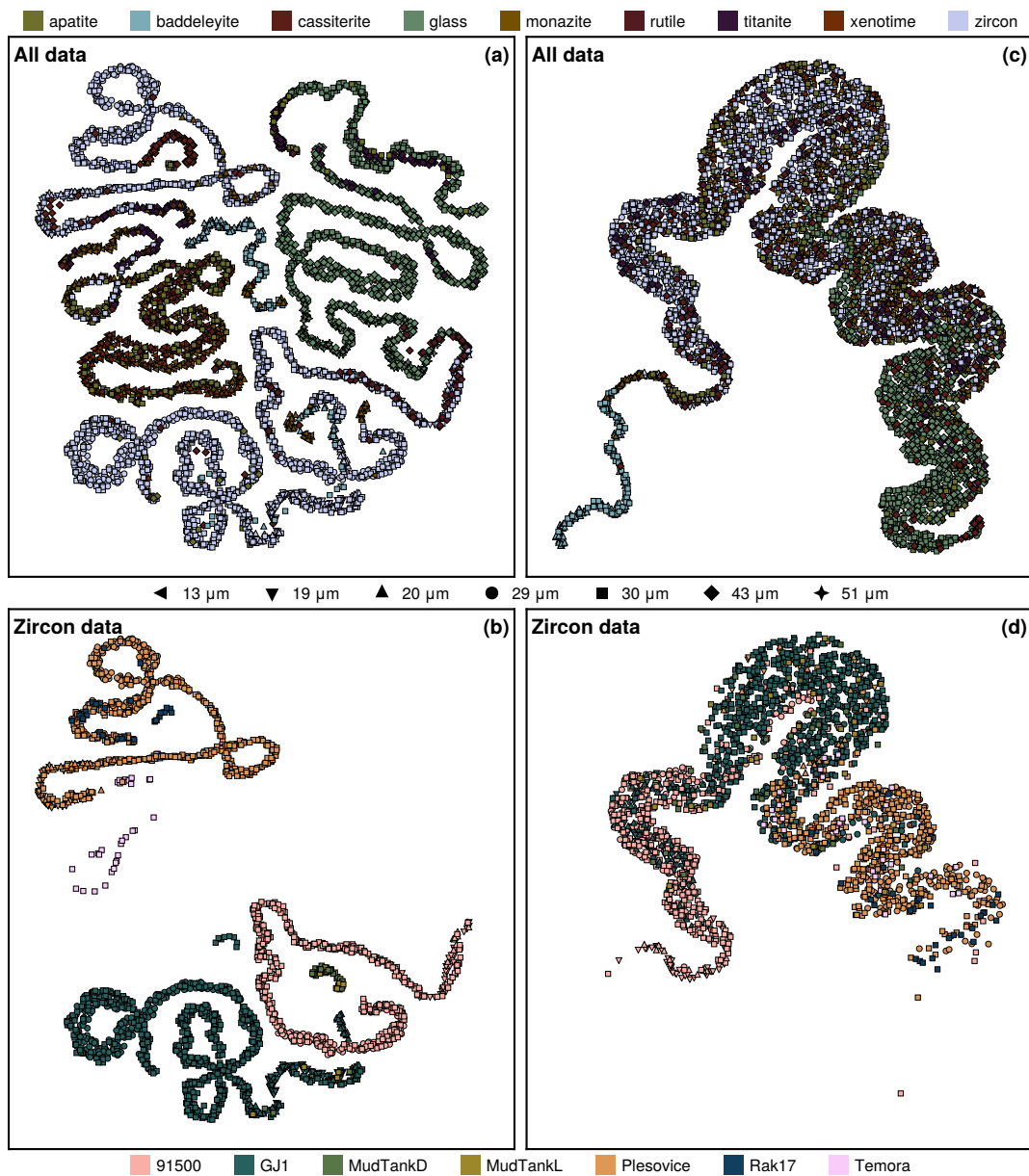
Figure 7. (a) Uniform manifold approximation and project (UMAP) of λ coefficients 0 to 4 for all analysis data (non-centred) in the study. (b) subset of (a) only including zircon analyses. (c) and (d) UMAP of λ coefficients 1 to 4 for centred analysis data in the study with (d) being the zircon data subset of (c). In a practical sense, the closer/more clustered points are to each other the more similar they are. Axes are omitted, as x-y coordinates are a normalised distance metric value with no physical meaning. This method of data visualisation is to help an end user understand the relative similarities within large datasets. (a) and (b) are strongly controlled by the λ_0 component, while (c) and (d) are reflecting the shape parameters $\lambda_{1...4}$ of different materials.

3.3.1 Interpreting the (sample aggregated) data fits

Oxides generally have a greater linear slope component (λ_1) compared to other materials analysed, cassiterite being an exception [Fig. 5 and Fig. 6]. The glass (NIST SRM 610), cassiterite, and xenotime samples show the least overall DHF. Of note with the glass (NIST SRM 610) is we can clearly see the impact of spot diameter (thus geometry) on DHF. With decreasing spot diameter, the overall magnitude (linear slope) of DHF is increased [Fig. 6], but it also exacerbates the complex shape parameters (quadratic and cubic curvatures etc.).

There are two distinct groupings (accounting for different spot diameters) for baddeleyite, with one group being the samples from Phalaborwa, and the other group being the Kovdor sample [Fig. 6]. The cause of this stark disparity in baddeleyite DHF is unknown, but the Ti concentration is 9–14 times higher in the Phalaborwa samples than in the Kovdor samples. The obvious outliers in the apatite, cassiterite, and monazite subpanels of Fig. 6 are the Durango and Wilberforce apatite samples, CstT4370 cassiterite, and the Pilbara monazite sample. For the Pilbara monazite, some analyses show considerable variation in their Pb and U concentration (proxied by count rate; see supplementary figures available at figshare for signal plots). Excluding these analyses from the sample/session aggregated fit for the Pilbara monazite will reduce the polynomial confidence interval, and would improve the quality of the fit. However, this data is still analytically relevant and indicates that the Pilbara monazite may not be suitable to be a RM due to the variable ratio of Pb and U. For the Durango apatite, the flat DHF fit and larger uncertainty are due to low Pb counts, and for Wilberforce, the steeper linear DHF component and larger uncertainty are due to inclusion of several points from some analyses that are highly leveraging the fit, even with automated outlier removal being applied. For cassiterite, the relatively flat fits, and outlier (CstT4370) are generally due to low Pb and/or U counts, and greater scatter in the underlying data. The discrepancies and/or larger uncertainties in the lambda coefficients for materials of the same type provide a way to numerically check for outliers in RM data, prior to further data reduction, rather than needing a user to review all the data graphically. A user should still review their data via graphical means as well to check for spurious results.

3.3.2 Application of UMAP as a data visualisation aid

For this study, a UMAP diagram [Fig. 7] helps to visualise the relative similarities between the λ coefficients for the 5478 analyses. If there are relationships in the data, we expect them to correlate with the individual materials (e.g. NIST SRM 610 glass, GJ-1 zircon, Plešovice zircon), the type of material (e.g. glass, zircon, xenotime), laser parameters, or a combination of these factors and should thus plot in clusters on a UMAP diagram. The resulting map [Fig. 7] clearly differentiates the various materials better than the simple biplot [Fig. 5c], which suffers from over-plotting, obscuring any similarities/trends. The UMAP algorithm was not provided prior knowledge about the material, only the λ coefficients. Panels (a) and (b) of Fig. 7 are strongly controlled by the mean ratio (λ_1) as the UMAP algorithm was provided with lambda values from non-centred fits to aid the reader in understanding the general principle of these diagrams. Panels (c) and (d) of Fig. 7 are more useful in visualising the relationships of the shape parameters within the DHF models as the effects of mass-bias and drift are removed by providing the algorithm with the lambda values from centred fits.

For small, simple datasets, a simple bi-plot may suffice, but in larger datasets, and especially an inter-laboratory comparison where there is likely to be several hundred-thousand to millions of individual data points, a method such as UMAP should be employed to visualise the relationships of the data.

In Fig. 7, it is apparent that baddeleyite (pale blue-green markers in the upper panels) DHF is different to all other materials analysed in this study as the points are forming their own clusters (particularly Fig. 7(c)). The deviation by baddeleyite is also reflected in Fig. 5 where baddeleyite analyses are plotting to the far right of each subplot, indicating a much stronger linear slope fractionation component. What is also noticeable is that there is a large diversity in the DHF patterns of zircon [Fig. 7(b) and (d)], which in part is due to analytical noise as the individual points represent a single analysis and the fits have greater uncertainty as they are more susceptible to that noise. Nevertheless, in general 91500 is behaving most differently from all other zircons at a given spot diameter [Fig. 8], and Plešovice is behaving most like NIST SRM 610 of all the zircons [Fig. 7(c) and (d)]. We do not suggest that NIST SRM 610 glass is a suitable alternative to correct DHF for zircon (as seen in Fig. 6, and Fig. 1), rather that there is significant variation in the DHF of zircon standards, and therefore careful consideration should be given to applying appropriate zircon standards for analytical sessions depending on the unknown zircons to be analysed, and the time period used for signal integration (Guillong and Günther, 2002; Hergenröder, 2006a; Košler et al., 2005; Paton et al., 2010).

t
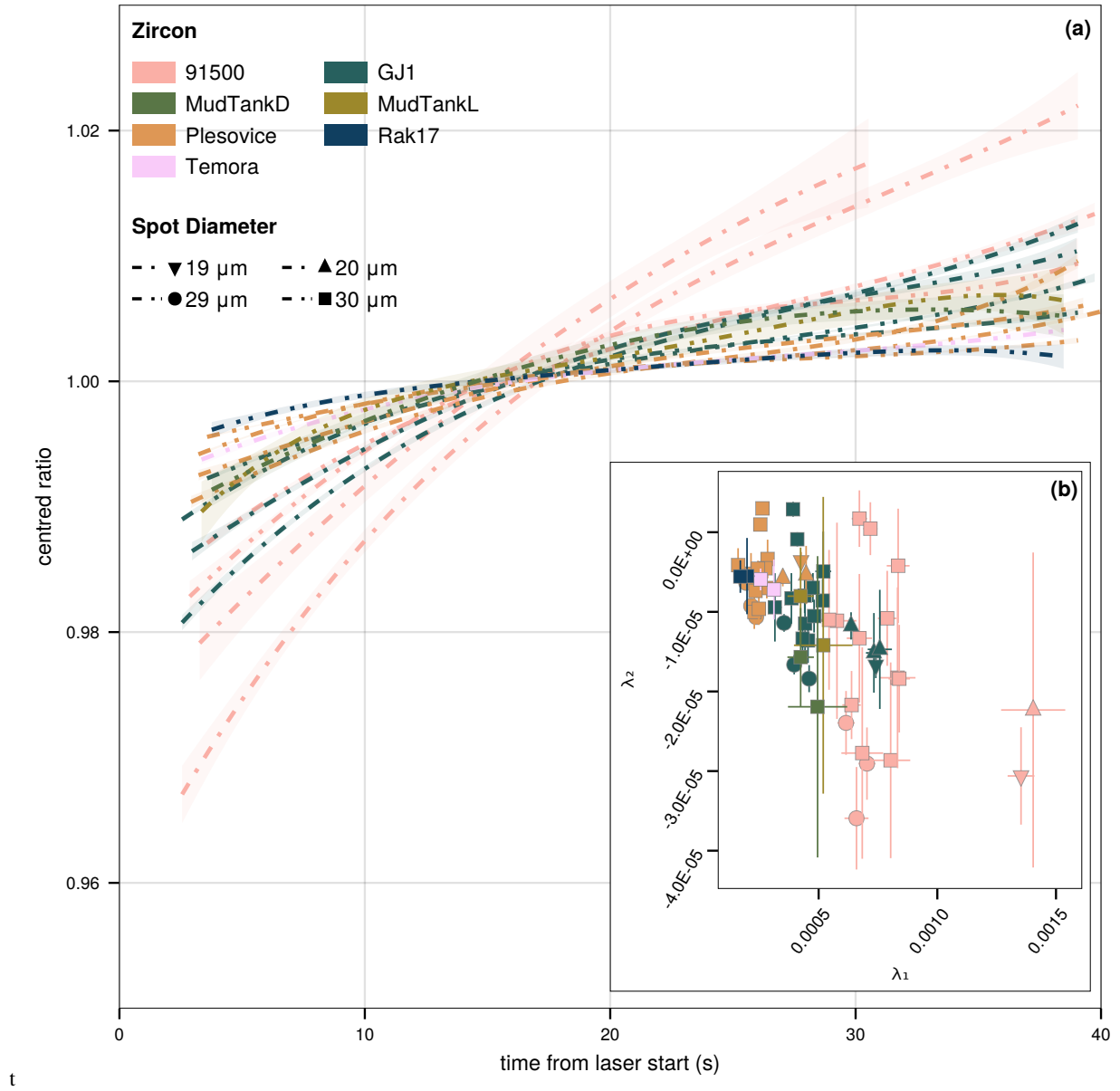
Figure 8. (a) Orthogonal polynomial fitting of down-hole fractionation for zircon data in this study. The visualised polynomials represent the best-order fit for the aggregated data of a given sample at a single spot diameter, e.g. GJ-1 at 30 μm, GJ-1 at 19 μm. Shaded areas show the 95% confidence interval of the individual fit. The inset graph (b) shows the λ_1 and λ_2 coefficients and their 2-standard error uncertainty for each of the session-based fits for the seven zircons analysed. Fits with a greater linear slope plot further to the right and fits with a greater negative quadratic curvature (i.e. the slope flattens at a faster rate) will plot toward the bottom

320   We can see that spot geometry has a significant impact on DHF [Fig. 6 (glass and zircon sub-panels), Fig. 7, and Fig. 8], which is a known phenomenon (Horn et al., 2000; Mank and Mason, 1999; Paton et al., 2010). However, all zircons except 91500 have remarkably similar DHF patterns at 29 μm (and 30 μm) [Fig. 8]. The linear slope component (λ_1) of the DHF pattern appears to be relatively constant between laser sessions for a given zircon and spot diameter, while the quadratic component varies (Fig. 8b) but has greater uncertainty associated with it. The exact mechanism as to why 91500 shows greater

325   DHF than the other analysed zircons is unknown, and not the focus of this manuscript; however, prior studies have investigated the potential causes of differing DHF patterns in zircon and glass (Košler et al., 2005), and it is possible that radiation damage plays a role (Allen and Campbell, 2012; Marillo-Sialer et al., 2014; Solari et al., 2015; Thompson et al., 2018).

3.4 Applications

The algorithm defined in this manuscript offers a way to numerically quantify processes in geoscience that can be modelled
330   with a linear combination of basis functions, building on the work of O'Neill (2016) and Anenburg and Williams (2022) with a more generalised approach. The generalised nature of this algorithm allows it to be used for orthogonal polynomial fitting, up to fourth order, of any data where is it sensible, i.e. there exists a polynomial of order $k_{(0...4)}$ that can model the input data. In this contribution we use it to numerically quantify DHF patterns of varied materials during LA-ICP-MS and demonstrate UMAP as a visualisation technique to help understand the structure of the data.

335   We envisage that this algorithm could be implemented in data reduction software to self-correct the DHF pattern of well-behaved materials (i.e. fitting a single geochemical zone), or as splines to geologically meaningful zonation, with a fallback to a known homogeneous material where the analysis signal is complex (e.g. due to complex zonation or inclusions). In the latter case, the user would need to select an appropriate material, and it would likely result in somewhat inaccurate correction in any case, thus impacting the accuracy of the final result [Fig. 1]. Self-correction would require modelling the individual analysis
340   signal, and using the orthogonal model to then correct the data for DHF observed in that analysis.

Alternatively the coefficients of the orthogonal models could be used to determine which RM DHF pattern best suits the unknown material DHF pattern. The quantification of the DHF pattern enables numeric assessment of fits to unknowns against fits of knowns to find the most similar material with respect to DHF and of the appropriate model order. For example, the AICc is minimised for the fourth order polynomial for NIST SRM 610 and the third order polynomial for most zircon RMs, we can
345   see this reflected visually in Fig. 2, Fig. 4, Fig. 6, and Fig. 8. Using the measures of fit provides users with a way to choose an appropriate model that accurately reflects the uncertainty and scatter, while minimising overfitting and the introduction of artefact errors. Additionally, the quantification done by this algorithm provides a way for laboratories to quantitatively compare the DHF behaviour of their RMs and analytical setup against other laboratories.

4   Conclusions

350   This contribution generalises the orthogonal polynomial decomposition algorithms of O'Neill (2016) and Anenburg and Williams (2022) to allow for modelling of processes in geoscience that can be represented by a linear combination of ba-

sis functions (predictable x-to-y relationships) beyond REE patterns while also using input uncertainties as weights for the models. Being written in the Julia programming language enables fast computation of many thousands of input files from data ingestion to model output.

355   We demonstrate quantitative modelling of DHF patterns observed during static spot LA-ICP-MS using the developed algorithm by applying it to an exemplar dataset of U–Pb RMs and guide the reader through data visualisation and interpretation of the derived coefficients. The algorithm provides the ability to quantitatively compare DHF for the same RMs across laboratories, differences between RMs, and differences between analytical setups.

    Furthermore, this algorithm could be implemented into data reduction programs to numerically assess the similarities and

360 fit qualities of DHF correction, ensuring more accurate corrections are made. It is possible that the algorithm could be used to self-correct the DHF pattern of a single analysis by first modelling it then using that model to correct the pattern so long as the assumption that the signal (or portion of) reflects a single, geologically meaningful zone holds. This allows a relaxation of the assumption that the DHF pattern of an unknown is the same as a specified RM by decoupling the correction from that material which can lead to improvements in accuracy and/or precision of the final result. More conservatively or in cases

365 where the assumption of a single geologically meaningful zone does not hold, models of the individual analyses can be used to quantitatively choose the most similar RM to use as a DHF correction material.

Code and data availability. The Julia package which implements the above algorithms is in early development, however it is available to all via GitHub at: github.com/jarredclloyd/GeochemistryTools.jl. Raw and derived data used in this study is freely available from figshare at: doi.org/10.25909/26778298. Code used to compile the raw data, fit the data, and generate the figures in this manuscript are freely available

370 from figshare at: doi.org/10.25909/26779255

Supplementary figures. Supplementary figures S01 and S02 detailing the automatic signal times algorithm employed in this manuscript, and example data it was tested on are available at doi.org/10.25909/27041821. Additional figures showing the individual analysis signals are also available from figshare at doi.org/10.25909/26778592. A plot exists for each sample for each session, with the arbitrary colours of each plot representing individual analyses.

375 **Appendix A: Algorithmic Mathematics**

LA-ICP-MS count data are strictly positive integers and follow a (discrete) Poisson distribution at low count level (e.g. gas blank), although eventually approximate a normal distribution at high count rate as implied by the central limit theorem (Bevington and Robinson, 2003). Data from a mass-spectrometer used for geochronology and/or elemental analysis are generally output in counts-per-second (CPS) not counts and violate the integer requirement of a discrete probability distribution. This

380 combined with the less intuitive and asymmetric scale parameters of geometric means has led to the use of normal statistics (e.g.

arithmetic means) for ratio computations. The use of normal statistics for gas blank measurements generally leads to overestimation (arithmetic mean) or underestimation (median if lots of 0 counts), and to a violation of the equality $A/B = (B/A)^{-1}$. This latter violation is commonly seen in U–Pb geochronology, where $^{206}\text{Pb}/^{238}\text{U} \neq \left(^{238}\text{U}/^{206}\text{Pb}\right)^{-1}$. Given that elemental count data and elemental ratios are compositional data and are strictly positive real values (i.e. positively skewed) which often

385 follow a log-normal distribution, a geometric mean is a more appropriate measure of the central tendency of the data. In our algorithm we use the geometric mean to compute the gas blank value. While geometric means are often used to address the problems above, we use a modified geometric mean to incorporate valid zero values which a standard geometric mean cannot. We will first review the standard geometric mean before detailing the modified version. The geometric mean is defined for a set of positive real numbers as Eq. (A1) (Habib, 2012; Feng et al., 2017),

390
$$G = \sqrt[N]{\prod_{i=1}^{N} x_i} \tag{A1}$$

where G is the geometric mean, N is the total count of data, and x_i is the i-th input value from $i = 1$ to $i = N$. Alternatively, it can be calculated by the arithmetic mean of the logarithm of the values [Eq. A2] and then raising the result to e [Eq. A3] (Habib, 2012; Kirkwood, 1979; Feng et al., 2017).

$$\log G = \frac{1}{N} \sum_{i=1}^{N} \log x_i \tag{A2}$$

395
$$G = e^{\log(G)} \tag{A3}$$

As computing the product of an arbitrarily large series of numbers can lead to overflow errors (Fernández et al., 2003; Polhill et al., 2006), and therefore inaccurate results, most geometric mean algorithms implement the second form where the arithmetic mean is calculated from the logarithm transformed data and raised to e. The logarithmic transformation requires that all $x_i > 0$. Additionally, as this is a multiplicative mean, when any $x_i = 0$, $G = 0$.

400 To overcome these limitations and obtain a more accurate estimate of the mean gas blank, we implement a geometric mean that accounts for zeros [Eq. A4]. This equation is effectively a weighted arithmetic mean of the geometric mean of the values > 0, and the geometric mean of the zeros, i.e. 0, with the weights equal to the number of values in each category (Habib, 2012),

$$\text{for } G \geq 0,\ G = \frac{n_+ G_+ + n_0 G_0}{N} = \frac{n_+}{N} G_+ \tag{A4}$$

405 where G_+ is the geometric mean of all $x_i > 0$, n_+ is the count of $x_i > 0$, G_0 is the geometric mean of all $x_i = 0$ (i.e. 0), and n_0 is the count of all $x_i = 0$. While this form of the geometric mean has its critics (de la Cruz and Kreft, 2018) we believe it provides a more accurate estimate of the true gas blank which should lie somewhere between 0 and the arithmetic mean which will bias the result to values > 0, and it avoids the issue of small constants being added to the data causing major changes in the geometric mean (Feng et al., 2017).

410   Although they cannot handle values of zero, we implement a geometric variance [Eq. A5], geometric standard deviation [Eq. A6], and standard error of the geometric mean [Eq. A7] (Kirkwood, 1979; de Carvalho, 2016).

$$\text{for } x > 0,\ \sigma_G^2 = e^{\sigma_{\log x}^2} \tag{A5}$$

$$\text{for } x > 0,\ \sigma_G = e^{\sigma(\log x)} \tag{A6}$$

$$\text{for } x > 0,\ \text{SE}_G = e^{SE_{\log x}} \tag{A7}$$

415   Where $\sigma_{\log x}^2$, $\sigma_{\log x}$ and $\text{SE}_{\log x}$ are, respectively, the variance, standard deviation, and standard error of the mean of the logarithms of $x_i > 0$. The $\sigma(\log x)$ can also be interpreted as average magnitude of the relative deviation from the geometric mean and $SE_{\log x}$(Chatfield et al., 2025). In geometric statistics, the measures of variance, standard deviation, and standard errors are a scale parameter. The corresponding uncertainty range of G for these statistics is asymmetric and denoted by $(G \times u; G \div u)$ where u is the corresponding statistic (e.g. σ^2, σ, SE).

420   ## A1   Orthogonal polynomial decomposition

We use orthogonal polynomial decomposition to fit a polynomial to analyte ratio data where the coefficients have physical meaning in relation to that data. This decomposition enables quantification of the shape parameters of a down-hole fractionation pattern. Integral to this process is the calculation of the orthogonal polynomials [Eq. (A8)] to be used to fit the final model.

$$\hat{y}(x_i) = \lambda_0 + \lambda_1 \varphi_1(x_i) + \lambda_2 \varphi_2(x_i) + \lambda_3 \varphi_3(x_i) + \lambda_4 \varphi_4(x_i) \tag{A8}$$

425   Our implementation can fit up to a fourth order polynomial and requires solving the orthogonal property of Eq. (A9) for each orthogonal function, $\varphi(x)$.

$$\sum [\varphi_j(x_i) \varphi_k(x_i)] = 0 \text{ for } j \neq k \tag{A9}$$

The functions $\varphi_{1\ldots4}$ are as follows:

$$\varphi_1 = x_i - \beta$$

430
$$\varphi_2 = (x_i - \gamma_1)(x_i - \gamma_2)$$

$$\varphi_3 = (x_i - \delta_1)(x_i - \delta_2)(x_i - \delta_3)$$

$$\varphi_4 = (x_i - \varepsilon_1)(x_i - \varepsilon_2)(x_i - \varepsilon_3)(x_i - \varepsilon_4)$$

Where β, γ_n, δ_n, ε_n are predetermined constants calculated prior to fitting the final model. The solution to β is simply the arithmetic mean of the x values [Eq. (A10)].

435
$$\sum_{i=1}^{N}(x_i - \beta) = 0, \text{ leading to } \frac{1}{N}\sum_{i=1}^{N}(x_i) = \beta \tag{A10}$$

The solutions to $\gamma_{1...2}$, $\delta_{1...3}$, $\varepsilon_{1...4}$ require solving systems of equations with increasing complexity as follows, with a line break between polynomial orders:

$$\sum (x_i - \gamma_1)(x_i - \gamma_2) = 0$$
$$\sum x_i (x_i - \gamma_1)(x_i - \gamma_2) = 0$$

440

$$\sum (x_i - \delta_1)(x_i - \delta_2)(x_i - \delta_3) = 0$$
$$\sum x_i (x_i - \delta_1)(x_i - \delta_2)(x_i - \delta_3) = 0$$
$$\sum x_i{}^2 (x_i - \delta_1)(x_i - \delta_2)(x_i - \delta_3) = 0$$

445

$$\sum (x_i - \varepsilon_1)(x_i - \varepsilon_2)(x_i - \varepsilon_3)(x_i - \varepsilon_4) = 0$$
$$\sum x_i (x_i - \varepsilon_1)(x_i - \varepsilon_2)(x_i - \varepsilon_3)(x_i - \varepsilon_4) = 0$$
$$\sum x_i{}^2 (x_i - \varepsilon_1)(x_i - \varepsilon_2)(x_i - \varepsilon_3)(x_i - \varepsilon_4) = 0$$
$$\sum x_i{}^3 (x_i - \varepsilon_1)(x_i - \varepsilon_2)(x_i - \varepsilon_3)(x_i - \varepsilon_4) = 0$$

This system of equations can be solved for numerically using an optimisation algorithm, or as stated in Anenburg and Williams

450 (2022) we can utilise Vieta's formulas to rearrange the complex system of equations to achieve an analytical solution. The application of Vieta's formula allows the conversion of the above complex systems to a simple polynomial whose real roots are the $\gamma_{1...2}$, $\delta_{1...3}$, and $\varepsilon_{1...4}$ values. Defining $\gamma_1 + \gamma_2 = a$ and $\gamma_1\gamma_2 = b$, and through simplification we obtain the matrix form of the following problem:

$$\begin{bmatrix} -\sum x_i & N \\ -\sum x_i{}^2 & \sum x_i \end{bmatrix} \begin{bmatrix} a \\ b \end{bmatrix} = \begin{bmatrix} -\sum x_i{}^2 \\ -\sum x_i{}^3 \end{bmatrix}$$

455 Once solved, a and b are the used as coefficients in the quadratic polynomial [Eq. (A11)] whose real roots are the two parameters γ_1 and γ_2.

$$\gamma^2 - a\gamma + b = 0 \tag{A11}$$

Following the same process, $\delta_{1...3}$ can be solved using Eq. (A12) and Eq. (A13), while $\varepsilon_{1...4}$ can be solved using Eq. (A14) and Eq. (A15).

$$\begin{bmatrix} -\sum x_i{}^2 & \sum x_i & -N \\ -\sum x_i{}^3 & \sum x_i{}^2 & -\sum x_i \\ -\sum x_i{}^4 & \sum x_i{}^3 & -\sum x_i{}^2 \end{bmatrix} \begin{bmatrix} a \\ b \\ c \end{bmatrix} = \begin{bmatrix} -\sum x_i{}^3 \\ -\sum x_i{}^4 \\ -\sum x_i{}^5 \end{bmatrix} \tag{A12}$$

$$\delta^3 - a\delta^2 + b\delta - c = 0 \tag{A13}$$

$$\begin{bmatrix} -\sum x_i{}^3 & \sum x_i{}^2 & -\sum x_i & N \\ -\sum x_i{}^4 & \sum x_i{}^3 & -\sum x_i{}^2 & \sum x_i \\ -\sum x_i{}^5 & \sum x_i{}^4 & -\sum x_i{}^3 & \sum x_i{}^2 \\ -\sum x_i{}^6 & \sum x_i{}^5 & -\sum x_i{}^4 & \sum x_i{}^3 \end{bmatrix} \begin{bmatrix} a \\ b \\ c \\ d \end{bmatrix} = \begin{bmatrix} -\sum x_i{}^4 \\ -\sum x_i{}^5 \\ -\sum x_i{}^6 \\ -\sum x_i{}^7 \end{bmatrix} \tag{A14}$$

$$\varepsilon^4 - a\varepsilon^3 + b\varepsilon^2 - c\varepsilon + d = 0 \tag{A15}$$

To account for errors in y (i.e. analyte ratios) we use generalised least-squares [Eq. A16] to fit the model. The errors in y are used as weights for the generalised least-squares algorithm. As we have not yet implemented input covariances, our model is the specialised case of generalised least-squares known as weighted least-squares.

let $y = \mathbf{X}\boldsymbol{\lambda} + \boldsymbol{\epsilon}$, $E[\boldsymbol{\epsilon}|\mathbf{X}]$, and $\mathrm{Cov}[\boldsymbol{\epsilon}|\mathbf{X}] = \sigma^2 \boldsymbol{\Omega} = \mathbf{U}$, then $\boldsymbol{\lambda} = \left(\mathbf{X}^\mathsf{T}\boldsymbol{\Omega}^{-1}\mathbf{X}\right)^{-1}\mathbf{X}^\mathsf{T}\boldsymbol{\Omega}^{-1}y$ and $\mathbf{U} = \left(\mathbf{X}^\mathsf{T}\boldsymbol{\Omega}^{-1}\mathbf{X}\right)^{-1}$ (A16)

To generate the orthogonal nature of the fit, the design matrix, $\mathbf{X}$, uses the $\varphi_{1...4}$ functions from above and is as follows:

$$\begin{bmatrix} 1 & \varphi_1(x_1) & \varphi_2(x_1) & \varphi_3(x_1) & \varphi_4(x_1) \\ 1 & \varphi_1(x_i) & \varphi_2(x_i) & \varphi_3(x_i) & \varphi_4(x_i) \\ \vdots & \vdots & \vdots & \vdots & \vdots \\ 1 & \varphi_1(x_n) & \varphi_2(x_n) & \varphi_3(x_n) & \varphi_4(x_n) \end{bmatrix}$$

Let the individual weights, ω_i, be the absolute error of y_i, then the weight matrix $\boldsymbol{\Omega}$ is as follows:

$$\begin{bmatrix} \omega_1^2 & & & \\ & \omega_i^2 & & \\ & & \ddots & \\ & & & \omega_n^2 \end{bmatrix}$$

The system can then be solved for the vector of coefficients, $\boldsymbol{\lambda}$, using Eq. (A16).

For true generalised least-squares, the non-diagonal elements of $\boldsymbol{\Omega}$ would be the covariances. Future improvements of the algorithm will implement covariance terms.

In the following equations, y_i is the i-th value of the observed dependant variable (e.g. analyte ratio), $\hat{y}_i$ is i-th value of the predicted dependant variable, n is the total number of values and k is the polynomial order. To assess the quality of fitted

models, and to assist with choosing an optimal model, we implemented several measures of fit. Standard measures of fit calculated are the residual sum of squares [rss, Eq. (A17)],

$$\text{rss}_k = \left(\sum_{i=1}^{n} \left(y_i - \hat{y}_{i_k} \right) \right)^{\mathsf{T}} \boldsymbol{\Omega}^{-1} \left(\sum_{i=1}^{n} \left(y_i - \hat{y}_{i_k} \right) \right) \tag{A17}$$

480 the mean-square error or reduced chi-squared value in multiple regression [mse or χ_r^2, Eq. (A18)],

$$\chi_{r_k}^2 = \text{mse}_k = \frac{\text{rss}}{n - k + 1} \tag{A18}$$

the root-mean-square error [rmse, Eq. (A19)],

$$\text{rmse}_k = \sqrt{\text{mse}_k} \tag{A19}$$

the normalised root-mean-square error [nrmse, Eq. (A20)],

485 $$\text{nrmse}_k = \frac{\text{rmse}_k}{\max y - \min y} \tag{A20}$$

and the multiple regression coefficient [ρ^2 or R^2, Eq. (A21)]

$$\rho^2 = 1 \frac{\text{rss}_k}{\left[y - \bar{y} \right]^{\mathsf{T}} \Omega \left[y - \bar{y} \right]} \tag{A21}$$

Additionally, we implement two measures based on Bayesian reasoning and information theory. The first of these is the corrected Bayesian (or Schwarz) information criterion [BICc, Eq. (A22)] and corresponding BICc weights [BICcW, Eq. (A23)]
490 (Burnham and Anderson, 2002; Schwarz, 1978).

$$\text{BICc}_k = n \log \left(\frac{\text{rss}}{n} \right) + (k + 2) \log (n) + \log (2\pi) + n \tag{A22}$$

$$\text{BICcW}_k = \frac{\exp \left(-0.5 \text{BICc}_k - \min \left[\text{BICc} \right] \right)}{\sum_0^{max(k)} \exp \left(-0.5 \text{BICc}_k - \min \left[\text{BICc} \right] \right)} \tag{A23}$$

The second is the corrected Akaike information criterion [AICc, Eq. (A24)] and corresponding AICc weights [AICcW, Eq. (A25)] (Akaike, 1974; Burnham and Anderson, 2002).

495 $$\text{AICc}_k = n \log \left(\frac{\text{rss}}{n} \right) + 2 (k + 2) + \frac{2 (k + 2) ([k + 2] + 1)}{n - (k + 2) - 1} \tag{A24}$$

$$\text{AICcW}_k = \frac{\exp \left(-0.5 \text{AICc}_k - \min \left[\text{AICc} \right] \right)}{\sum_0^{\max(k)} \exp \left(-0.5 \text{AICc}_k - \min \left[\text{AICc} \right] \right)} \tag{A25}$$

Finally, we implement an Olkin-Pratt adjusted multiple correlation coefficient [$\hat{\rho}_{OP}^2$, Eq. (A26)] which is the optimal unbiased estimator of ρ^2 (Karch, 2020; Olkin and Pratt, 1958).

$$\hat{\rho}_{OP}^2 \left(\rho^2 \right) = 1 - \frac{n - 3}{n - (k + 1) - 1} \left(1 - \rho^2 \right) {}_2F_1 \left(1, 1; \frac{n - (k + 1) - 1}{2}; 1 - \rho^2 \right) \tag{A26}$$

500   The Olkin-Pratt adjusted multiple correlation coefficient requires computation of the Gauss hypergeometric function, which is computationally non-trivial; however, Karch (2020) outlines the process to do this, and this is implemented as Eq. (A27) using the Taylor series expansion [Eq. (A28)] of the Gauss hypergeometric function (Pearson et al., 2017).

$$_2F_1\left(a, b; c; z\right) = \begin{cases} 0 & \text{if } z = 0 \\ \frac{c-1}{c-2} & \text{if } z = 1 \\ \sum_{j=0}^{\infty} \underbrace{\frac{(a)_j (b)_j}{(c)_j} \frac{1}{j!} z^j}_{T_j} & \text{if } 0 < z < 1 \end{cases} \tag{A27}$$

For the case, $0 < z < 1$, the Taylor series is truncated when either the ratio of the value for next term in the series and
505   the current sum of the series are less than or equal to the machine epsilon value for a Float64 type, or when the number of iterations (and thus terms) reaches 1000 [Eq. (A28)]. This will effectively truncate the series when the machine cannot resolve the difference between the change in successive terms.

Let $T_0 = 1$, $S_0 = 1$, $j = 1$ then for $1 < j < 1000$ and $\dfrac{T_{j+1}}{S_j} > \epsilon$

$$T_{j+1} = T_j \left[\frac{\frac{(a+j)(b+j)}{(c+j)z}}{(j+1)} \right] \text{ and } S_j = \sum_{j=1}^{j < 1000} S_0 + T_{j+1} \tag{A28}$$

510   ## A2   Outlier detection

We implement automated outlier removal based on the studentised residual. An outlier is considered to have a studentised residual ≥ 3 from the model with the polynomial order (k) that minimises the AICc. This outlier removal process is computationally intensive as it requires calculation of leverages h_{ii} which are the diagonal values of the projection matrix. The individual leverages are calculated using Eq. A29.

515   $$h_{ii} = \sum \mathbf{X}_{i,1\ldots k} \left[\mathbf{U}_{1\ldots k, 1\ldots k} \mathbf{X}_{1\ldots k, 1\ldots n}^{\mathsf{T}} \mathbf{\Omega}^{-1} \right] \tag{A29}$$

From the non-studentised residuals [Eq. A30] and the mean square error [mse, Eq. A18], the studentised residuals are calculated using Eq. A31.

$$r_i = y_i - \hat{y}_i \tag{A30}$$

520   $$s_i = \sqrt{\text{mse}\left(1 - h_{ii}\right)} \tag{A31}$$

If the user chooses this automated outlier removal, the algorithm will loop until either a) no studentised residuals are ≥ 3, or b) the loop has performed ten iterations.

Appendix B: Laser Conditions

Table B1. LA-ICP-MS parameters

Laboratory and Sample Preparation	
Laboratory name	Adelaide Microscropy
Sample type/mineral	Apatite, baddeleyite, cassiterite, glass, monazite, rutile, titanite, xenotime, zircon
Sample preparation	All new materials were mounted in 25 mm diameter round epoxy mounts then polished. Existing materials were in 25 mm diameter round epoxy mounts

Laser Ablation System	
Make, model, type	RESOlution-LR ArF excimer
Ablation cell and volume	Laurin Technic S155 laser
Laser wavelength (nm)	193 nm
Pulse width (ns)	20 ns
Fluence (Jcm^{-2})	Material dependent –see Table B2 below
Repetition rate (Hz)	5 Hz
Ablation duration (s)	30 and 40 (session dependent)
Spot diameter (μm)	Material dependent –see Table B2 below
Sampling mode/pattern	Static spot
Ablation gas	He, $1.0 \ Lmin^{-1}$
Carrier gas	Ar, $1.0 \ Lmin^{-1}$

ICP-MS Instrument	
Make, model, type	Agilent 8900x –no reaction gas mode
RF power (W)	1500
Torch depth (mm)	4–4.5
Masses measured	Mg24, Al27, Si29, P31, Ca43, Ti49, Fe57, Y89, Zr90, Nb93, Sn118, Ba137, La139, Ce140, Pr141, Nd146, Sm147, Eu153, Gd157, Tb159, Dy163, Ho165, Er166, Tm169, Yb172, Lu175, Hf178, Hg202, Pb204, Pb206, Pb207, Pb208, Th232, U235, U238

Data Processing	
Gas blank	30 second (25 seconds of signal used)
Other Information	Data processing to compute gas blank, raw ratios, and uncertainties was done using the algorithms outlined in this publication.

Table B2. Summary of laser conditions and materials analysed in each session

Session Date	Material	Spot Diameter (µm)	Repetition Rate (Hz)	Nominal Fluence (Jcm^{-2})	Measured Fluence (Jcm^{-2})	Ablation Time (seconds)
2020-02-24	zircon	29	5	2		30
2020-02-24	glass	29	5	3.5		30
2020-02-24	glass	51	5	3.5		30
2020-02-26	zircon	29	5	2		30
2020-02-26	glass	29	5	3.5		30
2020-02-26	glass	51	5	3.5		30
2020-05-06	zircon	19	5	2		40
2020-05-06	glass	19	5	3.5		40
2020-05-06	glass	51	5	3.5		40
2020-05-08	glass	43	5	3.5		40
2020-05-11	zircon	29	5	2		40
2020-05-11	glass	29	5	3.5		40
2020-05-11	glass	51	5	3.5		40
2021-03-30	zircon	29	5	2		30
2021-03-30	glass	43	5	3.5		30
2021-03-31	zircon	30	5	2		40
2021-03-31	glass	43	5	3.5		40
2021-05-06	zircon	30	5	2		40
2021-05-06	glass	43	5	3.5		40
2021-09-06	zircon	30	5	2		30
2021-09-06	glass	43	5	3.5		30
2021-09-06	monazite	20	5	2		30
2022-01-19	baddeleyite	20	5	2		30
2022-01-19	zircon	20	5	2		30
2022-01-19	glass	43	5	3.5		30
2022-01-19	apatite	30	5	3.5		30
2022-02-01	monazite	13	5	2	1.9	30
2022-02-01	xenotime	13	5	2	1.9	30
2022-02-01	glass	43	5	3.5	3.6	30

Table B2. Summary of laser conditions and materials analysed in each session

Session Date	Material	Spot Diameter (µm)	Repetition Rate (Hz)	Nominal Fluence (Jcm^{-2})	Measured Fluence (Jcm^{-2})	Ablation Time (seconds)
2022-04-01	glass	43	5	3.5	3.4	30
2022-04-21	apatite	30	5	3.5	3.4	30
2022-04-21	zircon	30	5	2	2	30
2022-04-21	glass	43	5	3.5	3.4	30
2022-05-31	glass	43	5	5	5.2	30
2022-05-31	monazite	13	5	2	1.9	30
2022-05-31	xenotime	13	5	2	1.9	30
2022-06-20	zircon	30	5	2	2.1	30
2022-06-20	glass	43	5	3.5	3.6	30
2022-06-20	xenotime	13	5	2	2.1	30
2022-06-29	glass	43	5	3.5	3.4	30
2022-06-29	xenotime	13	5	2	1.9	30
2022-07-08	glass	43	5	3.5	3.6	40
2022-07-08	rutile	43	5	5	5.2	40
2022-08-30	monazite	20	5	2	2	30
2022-08-30	zircon	20	5	2	2	30
2022-10-10	glass	43	5	3.5	3.4	30
2022-10-10	zircon	30	5	2	1.9	30
2022-10-11	glass	30	5	3.5	3.4	30
2022-10-11	zircon	43	5	2	1.9	30
2022-12-09	glass	43	5	3.5	3.5	40
2022-12-09	rutile	43	5	5	4.9	40
2023-02-20	apatite	30	5	3.5	3.5	30
2023-02-20	glass	30	5	3.5	3.5	30
2023-02-20	zircon	30	5	2	1.9	30
2023-03-22	monazite	13	5	2	1.8	30
2023-03-22	xenotime	13	5	2	1.8	30

Table B2. Summary of laser conditions and materials analysed in each session

Session Date	Material	Spot Diameter (μm)	Repetition Rate (Hz)	Nominal Fluence (Jcm^{-2})	Measured Fluence (Jcm^{-2})	Ablation Time (seconds)
2023-04-21	glass	43	5	3.5	3.5	30
2023-04-21	apatite	43	5	3.5	3.5	30
2023-04-21	zircon	30	5	2	2	30
2023-05-09	glass	43	5	3.5	3.5	40
2023-05-23	glass	43	5	3.5	3.6	40
2023-05-29	glass	43	5	3.5	3.4	30
2023-05-29	monazite	13	5	2	2.1	30
2023-06-30	glass	30	5	3.5	3.4	30
2023-06-30	apatite	30	5	3.5	3.4	30
2023-07-11	glass	43	5	3.5	3.5	40
2023-07-11	zircon	20	5	2	1.9	40
2023-11-24	apatite	30	5	3.5	3.5	30
2023-11-24	baddeleyite	30	5	2	2	30
2023-11-24	monazite	20	5	2	2	30
2023-11-24	rutile	43	5	5	4.9	30
2023-11-24	titanite	43	5	5	4.9	30
2023-11-24	xenotime	20	5	2	2	30
2023-11-24	zircon	30	5	2	2	30
2023-11-24	glass	30	5	3.5	3.5	30
2024-04-29	apatite	30	5	3.5	3.5	40
2024-04-29	baddeleyite	30	5	2	2.1	40
2024-04-29	cassiterite	43	5	5	5.1	40
2024-04-29	monazite	20	5	2	2.1	40
2024-04-29	rutile	43	5	5	5.1	40
2024-04-29	titanite	43	5	5	5.1	40
2024-04-29	xenotime	20	5	2	2.1	40
2024-04-29	zircon	30	5	2	2.1	40
2024-04-29	glass	30	5	3.5	3.5	40

Author contributions. **Jarred C. Lloyd**: Conceptualisation, data curation, formal analysis, investigation, methodology, resources, software, validation, visualisation, writing–original, writing–review & editing. **Carl Spandler**: Conceptualisation, resources, supervision, writing–review & editing. **Sarah E. Gilbert**: Formal analysis, methodology, resources, writing–review & editing. **Derrick Hasterok**: Methodology, validation, writing–review & editing.

Competing interests. The authors declare that they have no conflicts of interest.

Acknowledgements. We acknowledge and pay respects to the Kaurna People, the traditional custodians whose ancestral lands the University of Adelaide is built on, and we work on. We acknowledge the deep feelings of attachment and relationship of the Kaurna people to Country, and we respect and value their past, present and ongoing connection to the land and cultural beliefs.

The authors also acknowledge the Tate Museum and South Australian Museum for the provision of some sample material used in this study.

We thank the handling editor (Klaus Mezger), handling associate editor (Axel Schmitt), and referees (Noah McLean and one anonymous referee) for their constructive commentary that improved the manuscript.

Paul Olin and Mark Chatfield are thanked for their conversations regarding some concepts presented in this manuscript.

Financial support. This research was co-funded by the Australian Critical Minerals Research Centre at the University of Adelaide, and the Department for Energy and Mining, South Australia.

References

Agatemor, C. and Beauchemin, D.: Matrix Effects in Inductively Coupled Plasma Mass Spectrometry: A Review, Analytica Chimica Acta, 706, 66–83, https://doi.org/10.1016/j.aca.2011.08.027, 2011.

Akaike, H.: A New Look at the Statistical Model Identification, IEEE Transactions on Automatic Control, 19, 716–723, https://doi.org/10.1109/TAC.1974.1100705, 1974.

Allen, C. M. and Campbell, I. H.: Identification and Elimination of a Matrix-Induced Systematic Error in LA–ICP–MS 206Pb/238U Dating of Zircon, Chemical Geology, 332–333, 157–165, https://doi.org/10.1016/j.chemgeo.2012.09.038, 2012.

Anenburg, M. and Williams, M. J.: Quantifying the Tetrad Effect, Shape Components, and Ce–Eu–Gd Anomalies in Rare Earth Element Patterns, Mathematical Geosciences, 54, 47–70, https://doi.org/10.1007/s11004-021-09959-5, 2022.

Bevington, P. R. and Robinson, D. K.: Data Reduction and Error Analysis for the Physical Sciences, McGraw-Hill, Boston, 3rd ed edn., ISBN 978-0-07-247227-1, 2003.

Bezanson, J., Edelman, A., Karpinski, S., and Shah, V. B.: Julia: A Fresh Approach to Numerical Computing, SIAM Review, 59, 65–98, https://doi.org/10.1137/141000671, 2017.

Bockmann, M. J., Hand, M., Morrissey, L. J., Payne, J. L., Hasterok, D., Teale, G., and Conor, C.: Punctuated Geochronology within a Sustained High-Temperature Thermal Regime in the Southeastern Gawler Craton, Lithos, 430–431, 106 860, https://doi.org/10.1016/j.lithos.2022.106860, 2022.

Burnham, K. P. and Anderson, D. R.: Model Selection and Multimodel Inference: A Practical Information-Theoretic Approach, Springer, New York, 2nd ed edn., ISBN 978-0-387-95364-9, 2002.

Chatfield, M. D., Marquart-Wilson, L., Dobson, A. J., and Farewell, D. M.: Mean Relative Error and Standard Relative Deviation, Statistica Neerlandica, 79, e70 001, https://doi.org/10.1111/stan.70001, 2025.

Chew, D. M., Drost, K., and Petrus, J. A.: Ultrafast, > 50 Hz LA-ICP-MS Spot Analysis Applied to U–Pb Dating of Zircon and Other U-Bearing Minerals, Geostandards and Geoanalytical Research, 43, 39–60, https://doi.org/10.1111/ggr.12257, 2019.

Crameri, F., Shephard, G. E., and Heron, P. J.: The Misuse of Colour in Science Communication, Nature Communications, 11, 5444, https://doi.org/10.1038/s41467-020-19160-7, 2020.

Danisch, S. and Krumbiegel, J.: Makie.Jl: Flexible High-Performance Data Visualization for Julia, Journal of Open Source Software, 6, https://doi.org/10.21105/joss.03349, 2021.

de Carvalho, M.: Mean, What Do You Mean?, The American Statistician, 70, 270–274, https://doi.org/10.1080/00031305.2016.1148632, 2016.

de la Cruz, R. and Kreft, J.-U.: Geometric Mean Extension for Data Sets with Zeros, https://doi.org/10.48550/ARXIV.1806.06403, 2018.

Feng, C., Hongyue, W., Yun, Z., Yu, H., Yuefeng, L., and Tu, X. M.: Generalized Definition of the Geometric Mean of a Non Negative Random Variable, Communications in Statistics - Theory and Methods, 46, 3614–3620, https://doi.org/10.1080/03610926.2015.1066818, 2017.

Fernández, J.-J., García, I., and Garzón, E. M.: Floating Point Arithmetic Teaching for Computational Science, Future Generation Computer Systems, 19, 1321–1334, https://doi.org/10.1016/S0167-739X(03)00090-6, 2003.

Fletcher, I. R., McNaughton, N. J., Aleinikoff, J. A., Rasmussen, B., and Kamo, S. L.: Improved Calibration Procedures and New Standards for U–Pb and Th–Pb Dating of Phanerozoic Xenotime by Ion Microprobe, Chemical Geology, 209, 295–314, https://doi.org/10.1016/j.chemgeo.2004.06.015, 2004.

Gain, S. E. M., Gréau, Y., Henry, H., Belousova, E., Dainis, I., Griffin, W. L., and O'Reilly, S. Y.: Mud Tank Zircon: Long-Term Evaluation of a Reference Material for U-Pb Dating, Hf-Isotope Analysis and Trace Element Analysis, Geostandards and Geoanalytical Research, 43, 339–354, https://doi.org/10.1111/ggr.12265, 2019.

Gehrels, G. E., Valencia, V. A., and Ruiz, J.: Enhanced Precision, Accuracy, Efficiency, and Spatial Resolution of U-Pb Ages by Laser Ablation-Multicollector-Inductively Coupled Plasma-Mass Spectrometry, Geochemistry, Geophysics, Geosystems, 9, https://doi.org/10.1029/2007gc001805, 2008.

Gilbert, S. E., Olin, P., Thompson, J., Lounejeva, E., and Danyushevsky, L.: Matrix Dependency for Oxide Production Rates by LA-ICP-MS, Journal of Analytical Atomic Spectrometry, 32, 638–646, https://doi.org/10.1039/C6JA00395H, 2017.

Glorie, S., March, S., Nixon, A., Meeuws, F., O'Sullivan, G. J., Chew, D. M., Kirkland, C. L., Konopelko, D., and De Grave, J.: Apatite U–Pb Dating and Geochemistry of the Kyrgyz South Tian Shan (Central Asia): Establishing an Apatite Fingerprint for Provenance Studies, Geoscience Frontiers, https://doi.org/10.1016/j.gsf.2020.06.003, 2020.

Glorie, S., Mulder, J., Hand, M., Fabris, A., Simpson, A., and Gilbert, S.: Laser Ablation (in Situ) Lu-Hf Dating of Magmatic Fluorite and Hydrothermal Fluorite-Bearing Veins, Geoscience Frontiers, p. 101629, https://doi.org/10.1016/j.gsf.2023.101629, 2023.

Guillong, M. and Günther, D.: Effect of Particle Size Distribution on ICP-induced Elemental Fractionation in Laser Ablation-Inductively Coupled Plasma-Mass Spectrometry, Journal of Analytical Atomic Spectrometry, 17, 831–837, https://doi.org/10.1039/B202988J, 2002.

Günther, D., Frischknecht, R., Heinrich, C. A., and Kahlert, H.-J.: Capabilities of an Argon Fluoride 193 Nm Excimer Laser for LaserAblation Inductively Coupled Plasma Mass Spectometry Microanalysis ofGeological Materials, Journal of Analytical Atomic Spectrometry, 12, 939–944, https://doi.org/10.1039/A701423F, 1997.

Günther, D., v. Quadt, A., Wirz, R., Cousin, H., and Dietrich, V. J.: Elemental Analyses Using Laser Ablation-Inductively Coupled Plasma-Mass Spectrometry (LA-ICP-MS) of Geological Samples Fused with Li2B4O7 and Calibrated Without Matrix-Matched Standards, Microchimica Acta, 136, 101–107, https://doi.org/10.1007/s006040170038, 2001.

Habib, E. A. E.: Geometric Mean for Negative and Zero Values, International Journal of Research and Reviews in Applied Sciences, 11, 419–432, 2012.

Hall, J. W., Glorie, S., Reid, A. J., Boone, S. C., Collins, A. S., and Gleadow, A.: An Apatite U–Pb Thermal History Map for the Northern Gawler Craton, South Australia, Geoscience Frontiers, 9, 1293–1308, https://doi.org/10.1016/j.gsf.2017.12.010, 2018.

Hergenröder, R.: A Model of Non-Congruent Laser Ablation as a Source of Fractionation Effects in LA-ICP-MS, Journal of Analytical Atomic Spectrometry, 21, 505–516, https://doi.org/10.1039/B600698A, 2006a.

Hergenröder, R.: Hydrodynamic Sputtering as a Possible Source for Fractionation in LA-ICP-MS, Journal of Analytical Atomic Spectrometry, 21, 517–524, https://doi.org/10.1039/B600705H, 2006b.

Hirata, T. and Nesbitt, R. W.: U-Pb Isotope Geochronology of Zircon: Evaluation of the Laser Probe-Inductively Coupled Plasma Mass Spectrometry Technique, Geochimica et Cosmochimica Acta, 59, 2491–2500, https://doi.org/10.1016/0016-7037(95)00144-1, 1995.

Hogmalm, K. J., Zack, T., Karlsson, A. K. O., Sjöqvist, A. S. L., and Garbe-Schönberg, D.: In Situ Rb–Sr and K–Ca Dating by LA-ICP-MS/MS: An Evaluation of N2O and SF6 as Reaction Gases, Journal of Analytical Atomic Spectrometry, 32, 305–313, https://doi.org/10.1039/c6ja00362a, 2017.

Horn, I., Rudnick, R. L., and McDonough, W. F.: Precise Elemental and Isotope Ratio Determination by Simultaneous Solution Nebulization and Laser Ablation-ICP-MS: Application to U–Pb Geochronology, Chemical Geology, 164, 281–301, https://doi.org/10.1016/S0009-2541(99)00168-0, 2000.

Horstwood, M. S. A., Foster, G. L., Parrish, R. R., Noble, S. R., and Nowell, G. M.: Common-Pb Corrected in Situ U–Pb Accessory Mineral Geochronology by LA-MC-ICP-MS, Journal of Analytical Atomic Spectrometry, 18, 837–846, https://doi.org/10.1039/B304365G, 2003.

615 Horstwood, M. S. A., Košler, J., Gehrels, G. E., Jackson, S. E., McLean, N. M., Paton, C., Pearson, N. J., Sircombe, K. N., Sylvester, P., Vermeesch, P., Bowring, J. F., Condon, D. J., and Schoene, B.: Community-Derived Standards for LA-ICP-MS U-(Th-)Pb Geochronology - Uncertainty Propagation, Age Interpretation and Data Reporting, Geostandards and Geoanalytical Research, 40, 311–332, https://doi.org/10.1111/j.1751-908X.2016.00379.x, 2016.

Karch, J.: Improving on Adjusted R-Squared, Collabra: Psychology, 6, 45, https://doi.org/10.1525/collabra.343, 2020.

620 Kendall-Langley, L. A., Kemp, A. I. S., Grigson, J. L., and Hammerli, J.: U-Pb and Reconnaissance Lu-Hf Isotope Analysis of Cassiterite and Columbite Group Minerals from Archean Li-Cs-Ta Type Pegmatites of Western Australia, Lithos, 352–353, 105 231, https://doi.org/10.1016/j.lithos.2019.105231, 2020.

Kirkwood, T. B. L.: Geometric Means and Measures of Dispersion, Biometrics, 35, 908–909, https://www.jstor.org/stable/2530139, 1979.

Košler, J., Wiedenbeck, M., Wirth, R., Hovorka, J., Sylvester, P., and Míková, J.: Chemical and Phase Composition of Particles Produced by
625 Laser Ablation of Silicate Glass and Zircon—Implications for Elemental Fractionation during ICP-MS Analysis, J. Anal. At. Spectrom., 20, 402–409, https://doi.org/10.1039/B416269B, 2005.

Kroslakova, I. and Günther, D.: Elemental Fractionation in Laser Ablation-Inductively Coupled Plasma-Mass Spectrometry: Evidence for Mass Load Induced Matrix Effects in the ICP during Ablation of a Silicate Glass, Journal of Analytical Atomic Spectrometry, 22, 51–62, https://doi.org/10.1039/B606522H, 2006.

630 Larson, K. P., Dyck, B., Shrestha, S., Button, M., and Najman, Y.: On the Viability of Detrital Biotite Rb–Sr Geochronology, Geochronology, 6, 303–312, https://doi.org/10.5194/gchron-6-303-2024, 2024.

Liu, Z., Wu, F., Guo, C., Zhao, Z., Yang, J., and Sun, J.: In Situ U-Pb Dating of Xenotime by Laser Ablation (LA)-ICP-MS, Chinese Science Bulletin, 56, 2948–2956, https://doi.org/10.1007/s11434-011-4657-y, 2011.

Lloyd, J. C., Blades, M. L., Counts, J. W., Collins, A. S., Amos, K. J., Wade, B. P., Hall, J. W., Hore, S., Ball, A. L., Shahin, S.,
635 and Drabsch, M.: Neoproterozoic Geochronology and Provenance of the Adelaide Superbasin, Precambrian Research, 350, 105 849, https://doi.org/10.1016/j.precamres.2020.105849, 2020.

Lloyd, J. C., Collins, A. S., Blades, M. L., Gilbert, S. E., and Amos, K. J.: Early Evolution of the Adelaide Superbasin, Geosciences, 12, 154, https://doi.org/10.3390/geosciences12040154, 2022.

Lloyd, J. C., Preiss, W. V., Collins, A. S., Virgo, G. M., Blades, M. L., Gilbert, S. E., Subarkah, D., Krapf, C. B. E., and Amos,
640 K. J.: Geochronology and Formal Stratigraphy of the Sturtian Glaciation in the Adelaide Superbasin, Geological Magazine, pp. 1–24, https://doi.org/10.1017/S0016756823000390, 2023.

Lloyd, J. C., Collins, A. S., Blades, M. L., Gilbert, S. E., Mulder, J. A., and Amos, K. J.: Mid- to Late Neoproterozoic Development and Provenance of the Adelaide Superbasin, $\tau\epsilon\kappa\tau$oniκa, 2, 85–111, https://doi.org/10.55575/tektonika2024.2.2.65, 2024.

Mank, A. J. G. and Mason, P. R. D.: A Critical Assessment of Laser Ablation ICP-MS as an Analytical Tool for Depth Analysis in Silica-
645 Based Glass Samples, Journal of Analytical Atomic Spectrometry, 14, 1143–1153, https://doi.org/10.1039/A903304A, 1999.

Marillo-Sialer, E., Woodhead, J., Hergt, J., Greig, A., Guillong, M., Gleadow, A., Evans, N., and Paton, C.: The Zircon 'Matrix Effect': Evidence for an Ablation Rate Control on the Accuracy of U–Pb Age Determinations by LA-ICP-MS, Journal of Analytical Atomic Spectrometry, 29, 981–989, https://doi.org/10.1039/c4ja00008k, 2014.

McFarlane, C. R. M.: Allanite UPb Geochronology by 193 Nm LA ICP-MS Using NIST610 Glass for External Calibration., Chemical
650 Geology, 438, 91–102, https://doi.org/10.1016/j.chemgeo.2016.05.026, 2016.

McInnes, L., Healy, J., and Melville, J.: UMAP: Uniform Manifold Approximation and Projection for Dimension Reduction, https://doi.org/10.48550/arXiv.1802.03426, 2020.

McLean, N. M., Bowring, J. F., and Gehrels, G.: Algorithms and Software for U-Pb Geochronology by LA-ICPMS, Geochemistry, Geophysics, Geosystems, 17, 2480–2496, https://doi.org/10.1002/2015GC006097, 2016.

655 Mohammadi, N., Lentz, D. R., Thorne, K. G., Walker, J., Rogers, N., Cousens, B., and McFarlane, C. R. M.: U-Pb and Re-Os Geochronology and Lithogeochemistry of Granitoid Rocks from the Burnthill Brook Area in Central New Brunswick, Canada: Implications for Critical Mineral Exploration, Geochemistry, p. 126087, https://doi.org/10.1016/j.chemer.2024.126087, 2024.

Norris, A. and Danyushevsky, L.: Towards Estimating the Complete Uncertainty Budget of Quantified Results Measured by LA-ICP-MS, 2018.

660 Olkin, I. and Pratt, J. W.: Unbiased Estimation of Certain Correlation Coefficients, The Annals of Mathematical Statistics, 29, 201–211, https://doi.org/10.1214/aoms/1177706717, 1958.

O'Neill, H. S. C.: The Smoothness and Shapes of Chondrite-normalized Rare Earth Element Patterns in Basalts, Journal of Petrology, 57, 1463–1508, https://doi.org/10.1093/petrology/egw047, 2016.

Paton, C., Woodhead, J. D., Hellstrom, J. C., Hergt, J. M., Greig, A., and Maas, R.: Improved Laser Ablation U-Pb Zircon Geochronology

665 through Robust Downhole Fractionation Correction, Geochemistry, Geophysics, Geosystems, 11, https://doi.org/10.1029/2009GC002618, 2010.

Paton, C., Hellstrom, J., Paul, B., Woodhead, J., and Hergt, J.: Iolite: Freeware for the Visualisation and Processing of Mass Spectrometric Data, Journal of Analytical Atomic Spectrometry, 26, 2508–2518, https://doi.org/10.1039/C1JA10172B, 2011.

Payne, J. L., Hand, M., Barovich, K. M., and Wade, B. P.: Temporal Constraints on the Timing of High-Grade Metamorphism in the

670 Northern Gawler Craton: Implications for Assembly of the Australian Proterozoic, Australian Journal of Earth Sciences, 55, 623–640, https://doi.org/10.1080/08120090801982595, 2008.

Pearson, J. W., Olver, S., and Porter, M. A.: Numerical Methods for the Computation of the Confluent and Gauss Hypergeometric Functions, Numerical Algorithms, 74, 821–866, https://doi.org/10.1007/s11075-016-0173-0, 2017.

Polhill, J. G., Izquierdo, L. R., and Gotts, N. M.: What Every Agent-Based Modeller Should Know about Floating Point Arithmetic, Envi-

675 ronmental Modelling & Software, 21, 283–309, https://doi.org/10.1016/j.envsoft.2004.10.011, 2006.

Roberts, N. M. W., Drost, K., Horstwood, M. S. A., Condon, D. J., Chew, D., Drake, H., Milodowski, A. E., McLean, N. M., Smye, A. J., Walker, R. J., Haslam, R., Hodson, K., Imber, J., Beaudoin, N., and Lee, J. K.: Laser Ablation Inductively Coupled Plasma Mass Spectrometry (LA-ICP-MS) U–Pb Carbonate Geochronology: Strategies, Progress, and Limitations, Geochronology, 2, 33–61, https://doi.org/10.5194/gchron-2-33-2020, 2020.

680 Schwarz, G.: Estimating the Dimension of a Model, Annals of Statistics, 6, 461–464, https://doi.org/10.1214/aos/1176344136, 1978.

Simpson, A., Gilbert, S., Tamblyn, R., Hand, M., Spandler, C., Gillespie, J., Nixon, A., and Glorie, S.: In-Situ Lu Hf Geochronology of Garnet, Apatite and Xenotime by LA ICP MS/MS, Chemical Geology, 577, https://doi.org/10.1016/j.chemgeo.2021.120299, 2021.

Sláma, J., Košler, J., Condon, D. J., Crowley, J. L., Gerdes, A., Hanchar, J. M., Horstwood, M. S. A., Morris, G. A., Nasdala, L., Norberg, N., Schaltegger, U., Schoene, B., Tubrett, M. N., and Whitehouse, M. J.: Plešovice Zircon — A New Natural Reference Material for U–Pb

685 and Hf Isotopic Microanalysis, Chemical Geology, 249, 1–35, https://doi.org/10.1016/j.chemgeo.2007.11.005, 2008.

Solari, L. A., Ortega-Obregón, C., and Bernal, J. P.: U–Pb Zircon Geochronology by LAICPMS Combined with Thermal Annealing: Achievements in Precision and Accuracy on Dating Standard and Unknown Samples, Chemical Geology, 414, 109–123, https://doi.org/10.1016/j.chemgeo.2015.09.008, 2015.

Spandler, C., Hammerli, J., Sha, P., Hilbert-Wolf, H., Hu, Y., Roberts, E., and Schmitz, M.: MKED1: A New Titanite Standard for in Situ Analysis of Sm–Nd Isotopes and U–Pb Geochronology, Chemical Geology, 425, 110–126, https://doi.org/10.1016/j.chemgeo.2016.01.002, 2016.

Subarkah, D., Blades, M. L., Collins, A. S., Farkaš, J., Gilbert, S., Löhr, S. C., Redaa, A., Cassidy, E., and Zack, T.: Unraveling the Histories of Proterozoic Shales through in Situ Rb-Sr Dating and Trace Element Laser Ablation Analysis, Geology, https://doi.org/10.1130/G49187.1, 2021.

Sylvester, P. J. and Ghaderi, M.: Trace Element Analysis of Scheelite by Excimer Laser Ablation-Inductively Coupled Plasma-Mass Spectrometry (ELA-ICP-MS) Using a Synthetic Silicate Glass Standard, Chemical Geology, 141, 49–65, https://doi.org/10.1016/S0009-2541(97)00057-0, 1997.

Tamblyn, R., Gilbert, S., Glorie, S., Spandler, C., Simpson, A., Hand, M., Hasterok, D., Ware, B., and Tessalina, S.: Molybdenite Reference Materials for In Situ LA-ICP-MS/MS Re-Os Geochronology, Geostandards and Geoanalytical Research, n/a, https://doi.org/10.1111/ggr.12550, 2024.

Thompson, J. M., Meffre, S., Maas, R., Kamenetsky, V., Kamenetsky, M., Goemann, K., Ehrig, K., and Danyushevsky, L.: Matrix Effects in Pb/U Measurements during LA-ICP-MS Analysis of the Mineral Apatite, Journal of Analytical Atomic Spectrometry, 31, 1206–1215, https://doi.org/10.1039/C6JA00048G, 2016.

Thompson, J. M., Meffre, S., and Danyushevsky, L.: Impact of Air, Laser Pulse Width and Fluence on U–Pb Dating of Zircons by LA-ICPMS, Journal of Analytical Atomic Spectrometry, 33, 221–230, https://doi.org/10.1039/C7JA00357A, 2018.

van der Wolff, E. J.: Detrital Provenance and Geochronology of the Burra, Umberatana and Wilpena Groups in the Mount Lofty Ranges, Honours Thesis, The University of Adelaide, Adelaide, South Australia, 2020.

Ver Hoeve, T. J., Scoates, J. S., Wall, C. J., Weis, D., and Amini, M.: Evaluating Downhole Fractionation Corrections in LA-ICP-MS U-Pb Zircon Geochronology, Chemical Geology, 483, 201–217, https://doi.org/10.1016/j.chemgeo.2017.12.014, 2018.

Wiedenbeck, M., Hanchar, J. M., Peck, W. H., Sylvester, P., Valley, J., Whitehouse, M., Kronz, A., Morishita, Y., Nasdala, L., Fiebig, J., Franchi, I., Girard, J. P., Greenwood, R. C., Hinton, R., Kita, N., Mason, P. R. D., Norman, M., Ogasawara, M., Piccoli, P. M., Rhede, D., Satoh, H., Schulz-Dobrick, B., Skår, O., Spicuzza, M. J., Terada, K., Tindle, A., Togashi, S., Vennemann, T., Xie, Q., and Zheng, Y. F.: Further Characterisation of the 91500 Zircon Crystal, Geostandards and Geoanalytical Research, 28, 9–39, https://doi.org/10.1111/j.1751-908X.2004.tb01041.x, 2004.

Yang, C.-X., Santosh, M., Lloyd, J., Glorie, S., Anilkumar, Y., Anoop, K. S., Gao, P., and Kim, S.-W.: Breakup of the Neoarchean Supercontinent Kenorland: Evidence from Zircon and Baddeleyite U-Pb Ages of LIP-related Mafic Dykes in the Coorg Block, Southern India, Geoscience Frontiers, p. 101804, https://doi.org/10.1016/j.gsf.2024.101804, 2024.

Zack, T., Stockli, D. F., Luvizotto, G. L., Barth, M. G., Belousova, E., Wolfe, M. R., and Hinton, R. W.: In Situ U–Pb Rutile Dating by LA-ICP-MS: 208Pb Correction and Prospects for Geological Applications, Contributions to Mineralogy and Petrology, 162, 515–530, https://doi.org/10.1007/s00410-011-0609-4, 2011.

Zhang, D. K.: Dzhang314/MultiFloats.Jl, https://github.com/dzhang314/MultiFloats.jl, 2024.